A&A 516, A46 (2010)
DOI: 10.1051/0004-6361/200913825

Astronomy & Astrophysics

The Hamburg/ESO *R*-process enhanced star survey (HERES)

V. Detailed abundance analysis of the *r*-process enhanced star HE 2327−5642⋆,⋆⋆

L. Mashonkina[1,2], N. Christlieb[3], P. S. Barklem[4], V. Hill[5], T. C. Beers[6], and A. Velichko[2]

[1] Universitäts-Sternwarte München, Scheinerstr. 1, 81679 München, Germany
e-mail: lyuda@usm.lmu.de
[2] Institute of Astronomy, Russian Academy of Sciences, 119017 Moscow, Russia
e-mail: lima@inasan.ru
[3] Zentrum für Astronomie der Universität Heidelberg, Landessternwarte, Königstuhl 12, 69117 Heidelberg, Germany
e-mail: N.Christlieb@lsw.uni-heidelberg.de
[4] Department of Astronomy and Space Physics, Uppsala University, Box 515, 75120 Uppsala, Sweden
[5] Observatoire de Paris, GEPI and URA 8111 du CNRS, 92195 Meudon Cedex, France
[6] Department of Physics and Astronomy, Michigan State University, East Lansing, MI 48824, USA

Received 8 December 2009 / Accepted 8 March 2010

ABSTRACT

Aims. We present a detailed abundance analysis of a strongly *r*-process enhanced giant star discovered in the HERES project, HE 2327−5642, for which [Fe/H] = −2.78, [r/Fe] = +0.99.
Methods. We determined the stellar parameters and element abundances by analyzing the high-quality VLT/UVES spectra. The surface gravity was calculated from the non-local thermodynamic equilibrium (NLTE) ionization balance between Fe I and Fe II, and Ca I and Ca II.
Results. Accurate abundances for a total of 40 elements and for 23 neutron-capture elements beyond Sr and up to Th were determined in HE 2327−5642. For every chemical species, the dispersion in the single line measurements around the mean does not exceed 0.11 dex. The heavy element abundance pattern of HE 2327−5642 is in excellent agreement with those previously derived for other strongly *r*-process enhanced stars, such as CS 22892-052, CS 31082-001, and HE 1219-0312. Elements in the range from Ba to Hf match the scaled Solar *r*-process pattern very well. No firm conclusion can be drawn about the relationship between the fisrt neutron-capture peak elements, Sr to Pd, in HE 2327−5642 and the Solar *r*-process, due to the uncertainty in the Solar *r*-process. A clear distinction in Sr/Eu abundance ratios was found between the halo stars of different europium enhancement. The strongly *r*-process enhanced stars contain a low Sr/Eu abundance ratio at [Sr/Eu] = −0.92 ± 0.13, while the stars with 0 < [Eu/Fe] < 1 and [Eu/Fe] < 0 have 0.36 dex and 0.93 dex higher Sr/Eu values, respectively. Radioactive dating for HE 2327−5642 with the observed thorium and rare-earth element abundance pairs results in an average age of 13.3 Gyr, when based on the high-entropy wind calculations, and 5.9 Gyr, when using the Solar *r*-residuals. We propose that HE 2327−5642 is a radial-velocity variable based on our high-resolution spectra covering ∼4.3 years.

Key words. stars: abundances – stars: atmospheres – stars: fundamental parameters – nuclear reactions, nucleosynthesis, abundances

1. Introduction

The detailed chemical abundances of Galactic halo stars contain unique information about the history and nature of nucleosynthesis in our Galaxy. A number of observational and theoretical studies have established that in the early Galaxy the rapid (*r*) process of neutron captures was primarily responsible for the formation of heavy elements beyond the iron group (we cite only the pioneering papers of Spite & Spite 1978; Truran 1981). The onset of the slow (*s*) process of neutron captures occurred at later Galactic times (and higher metallicities) with the injection of nucleosynthetic material from long-lived low- and intermediate-mass stars into the interstellar medium (see Travaglio et al. 1999, and references therein). Since 1994, a few rare stars have been found that exhibit large enhancements of the *r*-process elements, compared to Solar ratios, suggesting that their observed abundances are dominated by the influence of a single, or at most very few nucleosynthesis events. The *r*-process is associated with explosive conditions of massive-star core-collapse supernovae (Woosley et al. 1994), although the astrophysical site(s) of the *r*-process has yet to be identified. Observations of stars with strongly enhanced *r*-process elements have placed important constraints on the astrophysical site(s) of their synthesis.

Sneden et al. (1994) found that the extremely metal-poor ([Fe/H][1] ∼ −3.1) giant CS 22892-052 is neutron-capture-rich, [Eu/Fe]≃ +1.6 (following the suggestion of Beers & Christlieb 2005, we hereafter refer to stars having [Eu/Fe] > +1 and [Ba/Eu] < 0 as r-II stars), and that the relative abundances of nine elements in the range from Ba to Dy are consistent

⋆ Based on observations collected at the European Southern Observatory, Paranal, Chile (Proposal numbers 170.D-0010, and 280.D-5011).
⋆⋆ Table 8 is only available in electronic form at http://www.aanda.org

[1] In the classical notation, where [X/H] = $\log(N_X/N_H)_{star} - \log(N_X/N_H)_{Sun}$.

with a scaled Solar System *r*-process abundance distribution. Later studies of CS 31082-001 (Hill et al. 2002), BD+17° 3248 (Cowan et al. 2002), CS 22892-052 (Sneden et al. 2003), HD 221170 (Ivans et al. 2006), CS 22953-003 (François et al. 2007), HE 1219-0312, and CS 29491-069 (Hayek et al. 2009) provided strong evidence of a universal production ratio of the second *r*-process peak elements from Ba to Hf during the Galaxy history. CS 31082-001 (Hill et al. 2002) provided the first solid evidence that variations in progenitor mass, explosion energy, or other intrinsic and environmental factors or all of these may produce significantly different *r*-process yields in the actinide region ($Z \geq 90$). The third *r*-process peak ($76 \leq Z \leq 83$) has not been well constrained, because, in most r-II stars, it is only probed by abundance measurements of two elements, Os and Ir. The abundances of platinum and gold were obtained for CS 22892-052 (Sneden et al. 2003). The only detection of lead in a r-II star so far is in CS31082-001 (Plez et al. 2004).

Sneden et al. (2003) reported an underabundance of elements in the range of $40 < Z < 56$ relative to the scaled Solar *r*-process, which prompted a discussion of multiple *r*-process sites (see, for example, Travaglio et al. 2004; Qian & Wasserburg 2008; Farouqi et al. 2009). The detection of the radioactive elements thorium and uranium provided new opportunities for deriving the ages of the oldest stars and hence determining a lower limit to the age of the Universe (see the pioneering papers of Sneden et al. 1996; Cayrel et al. 2001). It appears that all the r-II stars with measured Th (and U) can be divided into two groups: (a) stars exhibiting an actinide boost (e.g., CS 31082-001, HE 1219-0312), and (b) stars with no obvious enhancement of thorium with respect to the scaled Solar *r*-process pattern (e.g., CS 22892-052, CS 29497-004; for a full list of stars, see Roederer et al. 2009). For the actinide boost stars, ages cannot be derived when only a single radioactive element, either Th or U, is detected.

To establish the origin of the heavy elements beyond the iron group in the oldest stars of the Galaxy, more numerous and accurate measurements of additional elements are required. Observations of only about ten r-II stars have been reported (Hill et al. 2002; Sneden et al. 2003; Christlieb et al. 2004; Honda et al. 2004; Barklem et al. 2005; François et al. 2007; Frebel et al. 2007; Lai et al. 2008; Hayek et al. 2009). The abundance pattern for a broad range of nuclei, based on high-resolution spectroscopic studies, have been reported for only six of these stars.

Continuing our series of papers on the Hamburg/ESO *R*-process-Enhanced Star survey (HERES), we aim to extend our knowledge of heavy element synthesis in the early Galaxy by means of a detailed abundance analysis of the strongly *r*-process enhanced star HE 2327−5642. We also investigate the reliability of multiple Th/*X* chronometers for HE 2327−5642, where *X* is an element in the Ba−Hf range.

HE 2327−5642 was identified as a candidate metal-poor star in the Hamburg/ESO Survey (HES; see Christlieb et al. (2008) for details of the candidate selection procedures). Moderate-resolution ($\Delta\lambda = 2$ Å) spectroscopy obtained at the Siding Spring Observatory (SSO) 2.3 m-telescope with the Double Beam Spectrograph (DBS) confirmed its metal-poor nature. Therefore, it was included in the target list of the HERES project. A detailed description of the project and its aims can be found in Christlieb et al. (2004, hereafter Paper I), and the methods of automated abundance analysis of high-resolution "snapshot" spectra were described in Barklem et al. (2005, hereafter Paper II). "Snapshot" spectra with a spectral resolution $R \sim 20\,000$ and a signal-to-noise ratio $S/N \sim 50$ per pixel at 4100 Å were used to show that HE 2327−5642 exhibits strong overabundances of the *r*-process elements, with [Eu/Fe] = +1.22 and [Ba/Eu] = −0.56 (Paper II).

This paper is structured as follows. After describing the observations in Sect. 2, we describe our abundance analysis of HE 2327−5642 in Sects. 3 and 4, based on high-quality VLT/UVES spectra and MAFAGS model atmospheres (Fuhrmann et al. 1997). The heavy element abundance pattern of HE 2327−5642 is discussed in Sect. 5. Section 6 reports on the radioactive decay age determination. Our conclusions are presented in Sect. 7.

Table 1. Coordinates and photometry of HE 2327−5642.

RA (2000.0)	23:30:37.2
dec (2000.0)	−56:26:14
V	13.881 ± 0.003
$B-V$	0.709 ± 0.005
$V-R$	0.456 ± 0.004
$V-I$	0.933 ± 0.005

Table 2. VLT/UVES observations of HE 2327−5642.

Setting	λ[1]	t_{exp}	S/N[2]
BLUE390	3330–4510 Å	4.0 h	10–65
BLUE437	3756–4978 Å	10.0 h	70–120
REDL580	4785–5745 Å	4.0 h	100–120
REDU580	5830–6795 Å	4.0 h	60–120
REDL860	6700–8508 Å	10.0 h	100–180

Notes. [(1)] λ refers to rest frame wavelengths, [(2)] S/N refers to the signal-to-noise ratio per pixel.

2. Observations

For the convenience of the reader, we list the coordinates and photometry of HE 2327−5642 in Table 1. The photometry was taken from Beers et al. (2007). High-quality spectra of this star was acquired during May–November 2005 with the VLT and UVES in dichroic mode. The BLUE390+RED580 (4 h total integration time) and BLUE437+RED860 (10 h) standard settings were employed to ensure a wide wavelength coverage. The slit width of 0.8″ in both arms yielded a resolving power of $R = 60\,000$. A 1 × 1 pixel binning ensured a proper sampling of the spectra. The observations are summarized in Table 2.

The pipeline-reduced spectra were shifted to the stellar rest frame and then coadded in an iterative procedure in which we identified pixels in the individual spectra affected by cosmic ray hits that had not been fully removed during the data reduction, or those affected by CCD defects or other artifacts. These pixels were flagged and ignored in the final iteration of the coaddition. Both sets of coadded blue spectra have S/N of at least 50 per pixel at $\lambda > 3800$ Å. At the shortest wavelengths, the S/N of the BLUE390 and BLUE437 is 10 (at 3330 Å) and 70 (at 3756 Å), respectively. The red arm spectra have $S/N > 100$ per pixel in most of the covered spectral range.

Barycentric radial velocities of HE 2327−5642 as measured with Gaussian fits of selected absorption lines in our high-resolution spectra, covering ∼4.3 years, indicate that the star is a radial-velocity variable, although no signatures of a double-lined spectroscopic binary star have been found. Our analysis of the data taken during the Modified Julian Date (MJD) period 53587.2−53666.2 (Table 3) infers that the radial velocity varies

Table 3. Barycentric radial velocities $v_{\rm rad,bary}$ of HE 2327−5642.

MJD* [days]	$v_{\rm rad,bary}$ [km s^{-1}]	σ^{**} [km s^{-1}]
52923.137	282	2
53587.172	282.2	0.3
53587.215	282.3	0.2
53587.257	282.3	0.3
53587.321	282.2	0.3
53592.289	281.3	0.3
53613.092	281.3	0.4
53613.135	281.5	0.5
53613.178	281.1	0.7
53613.221	281.4	0.6
53645.081	281.3	0.3
53653.044	282.4	0.2
53653.087	282.4	0.2
53666.112	284.1	0.2
53666.157	284.0	0.2
54407.020	302.4	0.3
54490.027	282.9	0.3

Notes. (*) The date refers to the start of the exposure.
(**) The error bars are the 1 σ scatter of the measurements based on different lines.

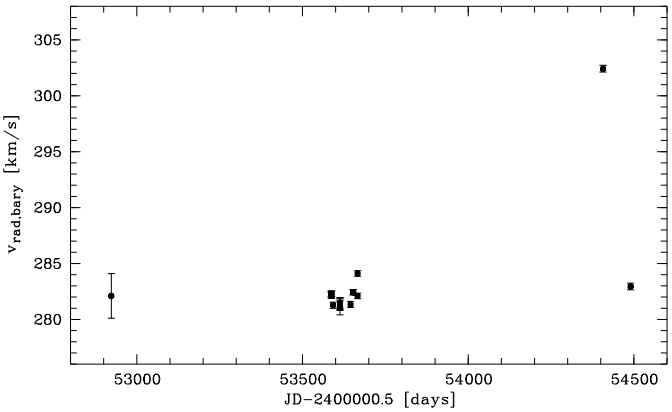

Fig. 1. Radial velocity measurements of HE 2327−5642.

on timescales of ∼10 days, and that the radial velocity curve underwent a minimum approximately at MJD 53620 (see Fig. 1). Furthermore, the measurement at MJD 54407.019 deviates by ∼20 km s^{-1} from the average of the radial velocities measured at the other epochs, and by a similar amount from the measurement taken only about three months later. The available data cannot be fitted satisfactorily by a sinusoidal curve, and we therefore suspect that the orbit of the system is highly elliptical. Additional observations are needed to confirm the variability, and to determine both the period and the nature of the orbit.

3. Analysis method

Our determinations of the stellar parameters and the elemental abundances are based on line profile and equivalent width analyses. We ignored any lines with equivalent widths larger than 100 mÅ. Exceptions were the elements, such as strontium, for which only strong lines can be detected in HE 2327−5642. For a number of chemical species, namely, H I, Na I, Mg I, Al I, Ca I-II, and Fe I-II, non-local thermodynamic equilibrium (NLTE) line formation was considered. The theoretical spectra of the remaining elements were calculated by assuming LTE. The coupled radiative transfer and statistical equilibrium equations were solved with the code NONLTE3 (Sakhibullin 1983; Kamp et al. 2003) for H I and Na I, and an updated version of the DETAIL code (Butler & Giddings 1985) for the remaining NLTE species. The departure coefficients were then used to calculate the synthetic line profiles with the code SIU (Reetz 1991). The metal linelist was extracted from the VALD database (Kupka et al. 1999). For molecular lines, we applied the data compiled by Kurucz (1994). To compare with observations, computed synthetic profiles were convolved with a profile that combines both the instrumental broadening with a Gaussian profile of 3.6 km s^{-1} and the broadening caused by macroturbulence. We employ the macroturbulence parameter $V_{\rm mac}$ in the radial-tangential form as prescribed in Gray (1992). By analyzing many line profiles in the spectrum of HE 2327−5642, $V_{\rm mac}$ = 3.3 km s^{-1} was empirically found with some allowance to vary by ±0.3 km s^{-1} (1σ).

The abundance analysis based on equivalent widths was performed with the code WIDTH9[2] (Kurucz 2004). The SIU and WIDTH9 codes both treat continuum scattering correctly, i.e., scattering is taken into account not only in the absorption coefficient, but also in the source function.

In both SIU and WIDTH9, we used the updated partition functions from the latest release of the MOOG code[3] (Sneden 1973), apart from those of Ho II and Ir II. For Ho II, we adopted the partition function calculated by Bord & Cowley (2002). The Ir II partition function was revised based on the measured energy levels of van Kleef & Metsch (1978). For the temperature range with which we are concerned, this produces a difference of +0.08/+0.2 dex in the Ho/Ir abundance determined from the Ho II/Ir I lines.

3.1. Stellar parameters and atmospheric models

In Paper II, an effective temperature of 5048 ± 100 K was derived from photometry when adopting the reddening derived from the maps of Schlegel et al. (1998). A subsequent analysis of the snapshot spectrum inferred that $\log g$ = 2.22 ± 0.25 and [Fe/H] = −2.95 ± 0.12. For the stellar parameter determination and abundance analysis, we used plane-parallel, LTE, and line-blanketed MAFAGS model atmospheres (Fuhrmann et al. 1997). Enhancements of the α-elements Mg, Si, and Ca by the amounts determined in a close-to-final iteration of our analysis were taken into account when computing these model atmospheres. Since suitable lines of oxygen were not covered by our spectra in hand, we could not determine the oxygen abundance, hence we adopted [O/Fe] = +0.5, which is typical of other stars of the same metallicity as HE 2327−5642. We note that oxygen in cool stellar atmospheres plays a minor role as both a donator of free electrons and an opacity source, hence an uncertainty in the oxygen abundance does not significantly affect the calculated atmospheric structure.

Heiter & Eriksson (2006) investigated the effect of geometry on atmospheric structure and line formation for Solar abundance models, and concluded that plane-parallel models can be applied in abundance analyses for stars with $\log g > 2$ and $T_{\rm eff} > 4000$ K. Therefore, HE 2327−5642 lies in the stellar parameter range where the usage of plane-parallel models is appropriate. This is confirmed by flux and abundance comparisons between a MAFAGS plane-parallel and MARCS (Gustafsson et al. 2008)[4] spherical models with stellar parameters close to those of HE 2327−5642, i.e., $T_{\rm eff}/\log g/$[M/H] = 5000/2.0/−3.

[2] http://kurucz.harvard.edu/programs/WIDTH/
[3] http://verdi.as.utexas.edu/moog.html
[4] http://marcs.astro.uu.se

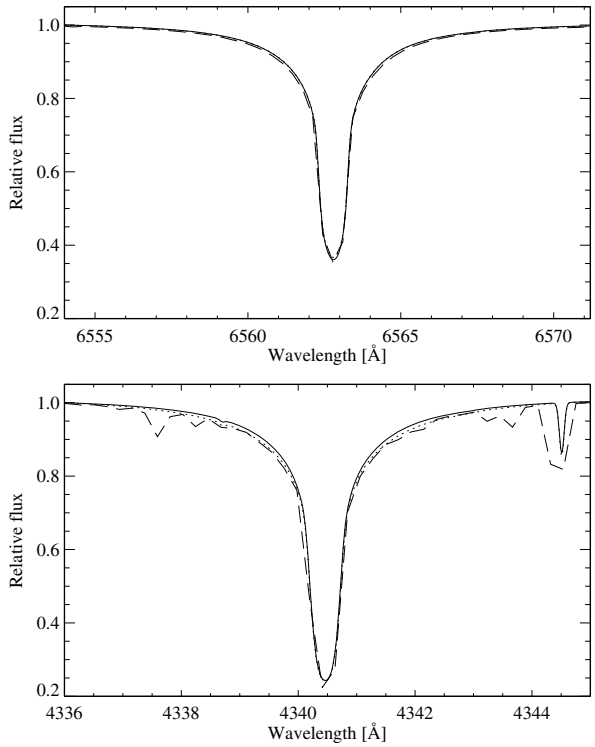

Fig. 2. Synthetic profiles of Hα (*top panel*) and Hγ (*bottom panel*) from the $s-s$ (dashed curve), $s-p$ (continuous curve), and $p-p$ (dotted curve) models. The calculations for the $s-p$ and $p-p$ models were made for pure hydrogen lines.

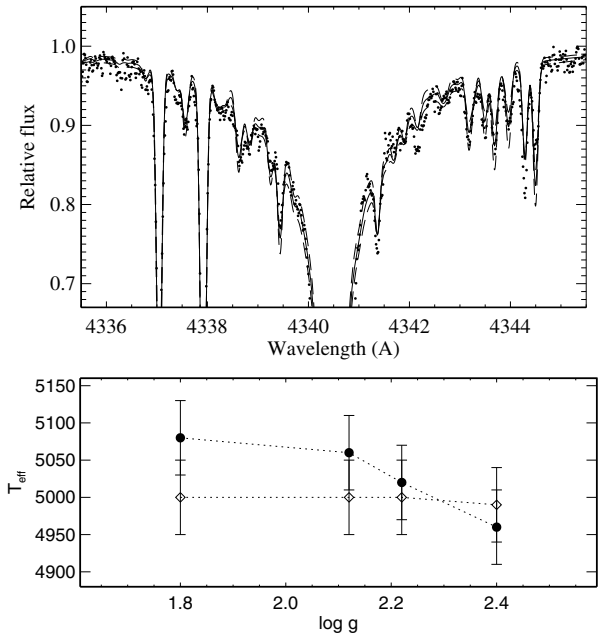

Fig. 3. *Top panel*: synthetic flux profile of Hγ computed for $T_{\rm eff}$ = 5000 K (continuous curve) compared to the observed spectrum of HE 2327−5642 (bold dots). The dashed curves show the effect of a 80 K variation in the effective temperature on the synthetic spectrum. In all calculations, we assumed $\log g$ = 2.3, [Fe/H] = −2.95, and ξ = 1.7 km s^{-1}. Bottom panel: effective temperature derived from the Hα (filled circles) and Hγ (open diamonds) line wings in HE 2327−5642 as a function of surface gravity. The error bars show the uncertainty of $T_{\rm eff}$ arising from profile fitting.

Synthetic spectra were computed for the wavelength range 3500−16 000 Å with the code SIU, which solves the equation of radiative transfer in only one depth variable. For the absolute flux, we compared three different combinations of model atmosphere and spectrum synthesis geometries i.e., consistently plane-parallel (MAFAGS + SIU, $p-p$), inconsistent (MARCS + SIU, $s-p$), and consistently spherical (MARCS model atmosphere library, $s-s$). The difference in absolute flux between these three models does not exceed 0.001 dex for wavelengths longer than 6600 Å. For $\lambda < 6600$ Å, the $p-p$ and $s-p$ fluxes are lower than those inferred from the $s-s$ model with a maximum difference of 0.01 dex and 0.02 dex, respectively, at wavelengths around 3500 Å.

In Fig. 2, we show the line profiles of Hα and Hγ for all three models. The Hγ profile of the MAFAGS model is consistent with that of the $s-s$ model. The difference in Hα relative fluxes between the MAFAGS and $s-s$ models translates into an effective temperature difference of 60 K. The abundance differences for the selected spectral lines were obtained between the $p-p$ and $s-p$ models by fitting the calculated synthetic spectra to the observed ones. The difference in absolute abundances, $\Delta \log \varepsilon((p-p)-(s-p))$, is always negative, but does not exceed 0.01 and 0.02 dex for the lines of neutral and ionized species, respectively. The differences in abundance ratios are also negligible; i.e., smaller than 0.01 dex.

The effective temperature of HE 2327−5642 was also determined from a profile analysis of Hα and Hγ based on NLTE line formation calculations of H I using the method described by Mashonkina et al. (2008). Only these two lines were employed because an accurate continuum rectification was not possible in the spectral regions covering other Balmer lines. The metallicity and microturbulence velocity from Paper II were adopted during the analysis of these Balmer lines, while the gravity was varied between $\log g$ = 1.8 and 2.4. The theoretical profiles of Hα and Hγ were computed by convolving the profiles resulting from the thermal, natural, and Stark broadening (Vidal et al. 1970, 1973), as well as self-broadening. For the latter, we use the self-broadening formalism of Barklem et al. (2000).

We found that NLTE has a weak effect on the Hγ profile beyond the core, because the difference between $T_{\rm eff}$ derived for this line assuming either NLTE or LTE does not exceed 20 K. We also found that the Hγ line wings are insensitive to a variation in surface gravity across the stellar parameter range with which we are concerned. The best fit solution was achieved at $T_{\rm eff}$ = 5000 K. Figure 3 (top panel) illustrates the quality of the fits.

Based on S/N of the observed spectrum and the sensitivity of the Balmer lines to variations on $T_{\rm eff}$, we estimate the uncertainty in $T_{\rm eff}$ arising from profile fitting to be 50 K for each line. For Hα, NLTE leads to a weakening of the core-to-wing transition relative to the LTE case, resulting in a $T_{\rm eff}$ that is 80−100 K higher depending on surface gravity. The effective temperature of HE 2327−5642 inferred from Hα also depends on $\log g$, as shown in the bottom panel of Fig. 3. The temperature deduced by combining the analyses of Hα and Hγ is $T_{\rm eff}$ = 5000 ± 70 K, and a favorable range of $\log g$ is that between 1.95 and 2.40.

The surface gravity and microturbulence velocity were redetermined from Ca and Fe lines based on NLTE line formation for Ca I-II and Fe I-II, using the methods of Mashonkina et al. (2007a, 2010). For Ca I-II, we employed the lines listed in Mashonkina et al. (2007a) along with the atomic data on gf−values and van der Waals damping constant. In total, 8 lines of Ca I and the only suitable Ca II line covered by our spectra, at 8498 Å, were used. For Fe I-II, 49 lines of Fe I and 8 lines of Fe II were selected from the linelists of Mashonkina et al. (2010),

Paper II, Jonsell et al. (2006), and Ivans et al. (2006). Van der Waals broadening of the Fe lines was accounted for using the most accurate data available from calculations of Anstee & O'Mara (1995); Barklem & O'Mara (1997, 1998); Barklem et al. (1998); Barklem & Aspelund-Johansson (2005). Hereafter, these collected papers by Anstee, Barklem, and O'Mara are referred to as the *ABO* theory. The lines used are listed in Table 8 (online material) with transition information, references for the adopted gf−values, and the final element abundances.

For Ca and Fe, we applied a line-by-line differential NLTE approach, in the sense that stellar line abundances were compared with individual abundances of their Solar counterparts. With the adopted atomic parameters, we note that the absolute Solar NLTE abundances obtained from the two ionization stages, Ca I and Ca II, Fe I and Fe II, were consistent within the error bars: $\log\varepsilon_\odot$(Ca I) = 6.36 ± 0.06, $\log\varepsilon_\odot$(Ca II 8498 Å) = 6.29, $\log\varepsilon_\odot$(Fe I) = 7.47 ± 0.10, and $\log\varepsilon_\odot$(Fe II) = 7.46 ± 0.07 (we refer to abundances on the usual scale, where $\log\varepsilon_H = 12$).

We performed NLTE computations for a small grid of model atmospheres with two effective temperatures, namely $T_{\rm eff}$ = 5050 K, derived from photometry, and $T_{\rm eff}$ = 4980 K, which is close to the result of the Balmer line analysis. In the statistical equilibrium calculations, inelastic collisions with hydrogen atoms were accounted for using the Steenbock & Holweger (1984) formula with a scaling factor of S_H = 0.1 for Ca and S_H = 1 for Fe, as recommended by Mashonkina et al. (2007a, 2010). The NLTE calculations for Ca I-II and Fe I-II were iterated for various elemental abundances until agreement between the theoretical and observed spectra was reached. The gravity was varied between $\log g$ = 1.8 and 2.6 in steps of 0.2 dex. Microturbulence values were tested in the range between ξ = 1.5 and 2.1 km s^{-1} in steps of 0.1 km s^{-1}. It was found that including the results for ξ = 1.5, 2.0, and 2.1 km s^{-1} produced a steep trend with measurable equivalent widths for the abundances found from individual Fe I lines, independent of the adopted values of $T_{\rm eff}$ and $\log g$, therefore these values were excluded.

Adopting $T_{\rm eff}$ = 5050 K, we obtained consistent iron abundances for the two ionization stages if $\log g$ = 2.34, 2.32, and 2.32, and ξ values of 1.7, 1.8, and 1.9 km s^{-1}, respectively. For Ca, this is achieved for $\log g$ = 2.28, 2.37, and 2.47. Figure 4 illustrates the determination of the surface gravity from the ionization equilibrium of Fe I/II and Ca I/II when the remaining stellar parameters are fixed at $T_{\rm eff}$ = 5050 K, [Fe/H] = −2.78, and ξ = 1.8 km s^{-1}. When adopting $T_{\rm eff}$ = 4980 K, the difference in $\log g$ obtained from Fe and Ca does not exceed 0.1 dex if ξ = 1.7 km s^{-1}. Thus, we identified two possible combinations of stellar parameters for HE 2327−5642: (a) 5050/2.34/−2.78 with ξ = 1.7−1.8 km s^{-1}, and (b) 4980/2.23/−2.85 with ξ = 1.7 km s^{-1} (see Fig. 5 for the combination 5050/2.34/−2.78). Both sets of the obtained parameters are consistent with each other within the uncertainties in the stellar parameters.

For consistency reasons, we adopted the effective temperature adopted in Paper II, i.e., $T_{\rm eff}$ = 5050 ± 70 K, and the other stellar parameters determined in this study, i.e., $\log g$ = 2.34 ± 0.1, [Fe/H] = −2.78 ± 0.09, and ξ = 1.8 ± 0.1 km s^{-1} (Table 4). For the derived effective temperature and surface gravity, the spectroscopic distance of HE 2327−5642 was estimated to range from 4.4 to 4.9 kpc for stellar mass of between 0.8 and 1 solar mass.

3.2. Line selection and atomic data

The lines used in the abundance analysis were selected from the lists of Paper II, Jonsell et al. (2006), Lawler et al. (2001c, 2004), Sneden et al. (2009), and Ivans et al. (2006). For atomic lines, we endeavored to apply single-source and recent gf-values wherever possible, to diminish the uncertainties involved by combining studies that may not be on the same gf-value system. For the selected lines of Na I, Mg I, Al I, Ca I-II, Sr II, and Ba II, we adopted gf-values (mostly from laboratory measurements) and van der Waals damping constants, which were carefully inspected in our previous analyses of the Solar spectrum (see Mashonkina et al. 2008 for references).

Fortunately, most neutron-capture element species considered here have been subjected to extensive laboratory investigations within the past two decades (Biémont et al. 1998; Den Hartog et al. 2003, 2006; Ivarsson et al. 2001, 2003; Lawler et al. 2001a,b,c, 2004, 2006, 2007, 2008, 2009; Ljung et al. 2006; Nilsson et al. 2002; Wickliffe & Lawler 1997b; Wickliffe et al. 2000; Xu et al. 2006). We employed gf−values determined by these laboratory efforts.

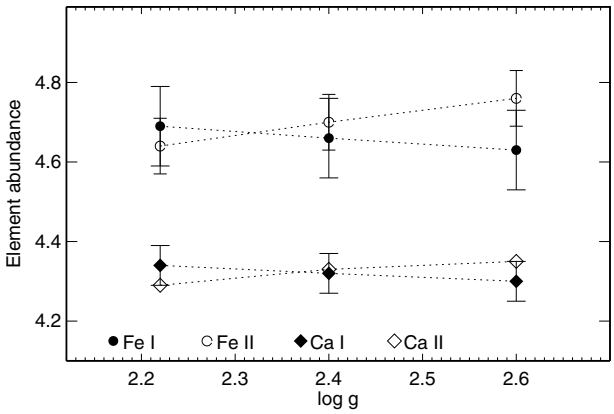

Fig. 4. NLTE abundances of Fe I (filled circles), Fe II (open circles), Ca I (filled diamonds), and Ca II (open diamonds) in HE 2327−5642 as a function of surface gravity. For clearer illustration, the symbols for Ca are shifted upwards by 0.5 dex. The calculations are for $T_{\rm eff}$ = 5050 K, [Fe/H] = −2.78, and ξ = 1.8 km s^{-1}.

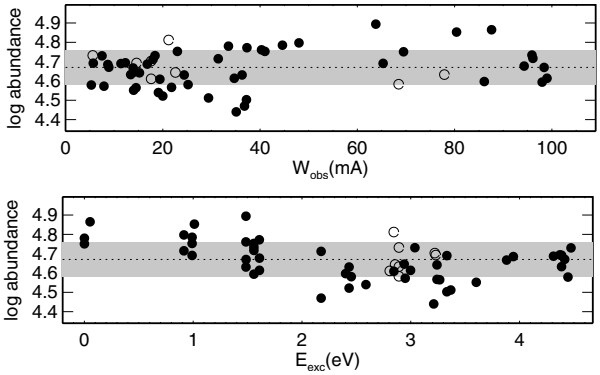

Fig. 5. Trends of abundances with equivalent width and excitation potential, as determined from individual Fe I (filled circles) and Fe II (open circles) lines, using our adopted stellar parameters. The dotted line indicates the mean Fe abundance from two ionization stages and the shaded grey area its statistical error.

Table 4. Determined stellar parameters of HE 2327−5642.

Parameter	Value	Uncertainty
$T_{\rm eff}$	5050 K	±70 K
$\log g$	2.34	±0.1
[Fe/H]	−2.78	±0.09
ξ	1.8 km s^{-1}	±0.1 km s^{-1}

Molecular data for two species, CH and NH, were assembled for the abundance determinations of carbon and nitrogen. For the analysis of the the $A - X$ bands at 4310−4313 Å and 4362−4367 Å, we used the CH line list of Paper II, and we use the ^{13}CH line list described in Hill et al. (2002). The NH molecular line data for the $A - X$ band at 3358−3361 Å was taken from Kurucz (1993).

The van der Waals damping for atomic lines was computed following the *ABO* theory, where the data were available, using the van der Waals damping constants Γ_6/N_H at 10 000 K as provided by the VALD database (Kupka et al. 1999). We note that the correct temperature dependence of the ABO theory was taken into account. An exception was the selected lines of some elements, for which we used the C_6-values derived from solar line-profile fitting by Gehren et al. (2004, Na I, Mg I, and Al I) and Mashonkina et al. (2008, Sr II and Ba II). If no other data were available, the Kurucz & Bell (1995) Γ_6/N_H values were employed.

Many elements considered here are represented by either a single isotope with an odd number of nucleons (Sc, Mn, Co, Pr, Tb, Ho, and Tm; ^{139}La accounts for 99.9% of lanthanum according to Lodders (2003)), or multiple isotopes with measured wavelength differences ($\Delta\lambda \geq 0.01$ Å for Ca II, Ba II, Nd II, Sm II, Eu II, Yb II, Ir I). Nucleon-electron spin interactions in odd-A isotopes lead to hyper-fine splitting (HFS) of the energy levels, resulting in absorption lines divided into multiple components. Without accounting properly for HFS and/or isotopic splitting (IS) structure, abundances determined from the lines sensitive to these effects can be severely overestimated. For example, in HE 2327−5642, including HFS makes a difference of −0.49 dex in the Ba abundance derived from the Ba II 4554 Å line, and including IS leads to a 0.13 dex lower Ca abundance for Ca II 8498 Å.

We present in Table 8 (online material) notes that indicate whether HFS/IS were considered in a given feature, and references to the HFS/IS data used. For a number of features, it was helpful to use the data for wavelengths and relative intensities of the HFS/IS components collected in the literature by Jonsell et al. (2006, Sc II, Mn I-II, Co I, La II, Tb II, Ho II, and Yb II), Ivans et al. (2006, Sc II and La II), Roederer et al. (2008, Nd II and Sm II), and Cowan et al. (2005, Ir I).

The selected lines are listed in Table 8 (online material), along with the transition information and references to the adopted gf-values.

Table 5. Summary of the abundances of HE 2327−5642.

Z	Species	$\log\varepsilon_\odot$	$N_{\rm lines}$	$\log\varepsilon$	$\sigma_{\log\varepsilon}$	[X/Fe]
3	Li I	1.10	1	0.99	–	
6	CH	8.39	4	5.74	0.01	0.13
7	NH	7.86	1	4.78	–	−0.20
11	Na I	6.30	2	2.92^N	0.05	−0.60
12	Mg I	7.54	3	4.95^N	0.04	0.19
13	Al I	6.47	1	3.02^N	–	−0.67
14	Si I	7.52	1	4.85	–	0.21
20	Ca I	6.33	8	3.83^N	0.05	0.28
20	Ca II	6.33	1	3.82^N	–	0.27
21	Sc II	3.10	4	0.10	0.02	−0.22
22	Ti I	4.90	10	2.14	0.08	0.12
22	Ti II	4.90	26	2.21	0.09	0.09
23	V II	4.00	4	0.89	0.08	−0.33
24	Cr I	5.64	6	2.32	0.11	−0.44
25	Mn I	5.37	1	1.89	–	−0.60
25	Mn II	5.37	3	1.98	0.10	−0.61
26	Fe I	7.45	49	4.66^N	0.10	−0.01
26	Fe II	7.45	8	4.68^N	0.07	0.01
27	Co I	4.92	6	1.96	0.08	−0.08
28	Ni I	6.23	8	3.10	0.10	−0.25
30	Zn I	4.62	2	1.83	0.01	0.09
38	Sr II	2.92	2	−0.01	0.00	−0.15
39	Y II	2.21	9	−0.69	0.06	−0.12
40	Zr II	2.58	12	0.04	0.05	0.24
42	Mo I	1.92	1	−0.49	–	0.47
46	Pd I	1.66	1	−0.72	–	0.50
56	Ba II	2.17	3	−0.30	0.03	0.31
57	La II	1.14	8	−1.10	0.02	0.54
58	Ce II	1.61	12	−0.63	0.06	0.54
59	Pr II	0.76	3	−1.15	0.06	0.87
60	Nd II	1.45	24	−0.61	0.08	0.72
62	Sm II	1.00	6	−0.92	0.09	0.86
63	Eu II	0.52	4	−1.29	0.02	0.98
64	Gd II	1.11	8	−0.72	0.07	0.95
65	Tb II	0.28	2	−1.51	0.03	0.99
66	Dy II	1.13	15	−0.60	0.06	1.05
67	Ho II	0.51	5	−1.31	0.10	0.96
68	Er II	0.96	11	−0.80	0.09	1.02
69	Tm II	0.14	5	−1.65	0.08	0.99
70	Yb II	0.86	1	−1.03	–	0.89
72	Hf II	0.88	1	−1.32	–	0.58
76	Os I	1.45	1	−0.17	–	1.26
77	Ir I	1.38	1	−0.05	–	1.45
90	Th II	0.08	1	−1.67	–	1.03

Notes. $^{(N)}$ NLTE abundance.

4. Abundance results

We derived the abundances of 40 elements from Li to Th in HE 2327−5642, and for four elements among them (Ca, Ti, Mn, and Fe), from two ionization stages. In Table 8 (online material), we list the results obtained from individual lines. For every feature, we provide the LTE abundance obtained and, for selected species, also the NLTE abundance. In Table 5, we list the mean abundances, the dispersion in the single line measurements about the mean ($\sigma_{\log\varepsilon}$), and the number of lines used to determine the mean abundances. We also list the Solar photosphere abundances, $\log\varepsilon_\odot$, adopted from Lodders et al. (2009), and the abundances relative to iron, [X/Fe]. For the computation of [X/Fe], $[{\rm Fe/H}]_{\rm NLTE} = -2.78$ was chosen as the reference, with the exception of the neutral species calculated based on a LTE assumption, where the reference is $[{\rm Fe\ I/H}]_{\rm LTE} = -2.88$. We comment below on individual groups of elements. The sample of cool giants from Cayrel et al. (2004) was chosen as our comparison sample.

4.1. Li and CNO

With an equivalent width of 15 mÅ, the Li I 6708 Å line is easily detected in this star. The abundance was determined using the spectrum synthesis approach, to account for the multiple-component structure of the line caused by both the fine structure of the upper energy level and the presence of two isotopes, ^{7}Li and ^{6}Li. The calculations of the synthetic spectra were performed in two ways: (a) without ^{6}Li, and (b) by adopting the Solar isotopic ratio, i.e., ^{7}Li: ^{6}Li = 92.4:7.6 (Lodders 2003). In both cases, the result for the Li abundance was $\log\varepsilon_{\rm LTE}({\rm Li}) = 0.99$. A goodness-of-fit analysis detected an asymmetry in the Li I 6708 Å line, which could be attributed to a weak ^{6}Li feature in the red wing of the ^{7}Li line. Although this asymmetry may

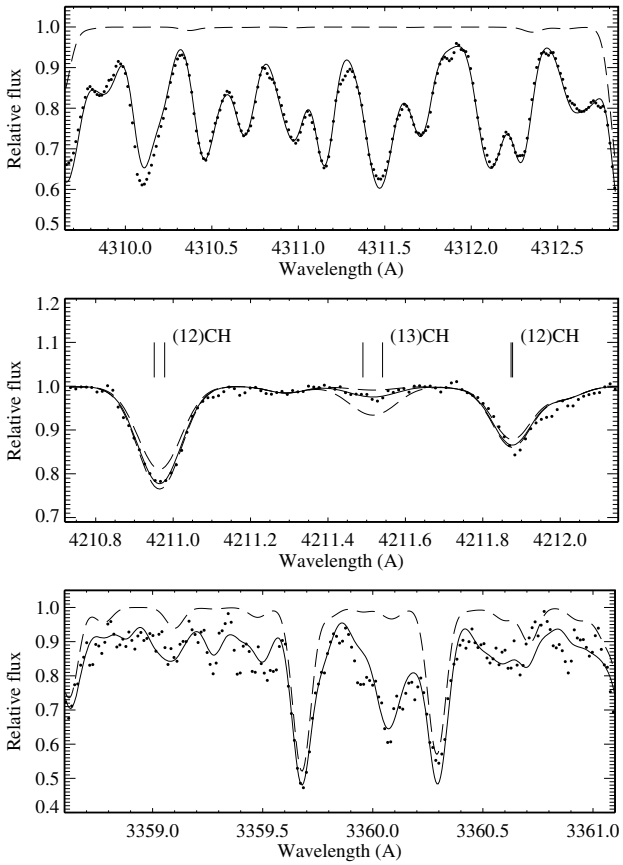

Fig. 6. Best fits (continuous curve) of the CH features near 4310 Å (*top panel*) and 4211 Å (*middle panel*), and the NH molecular band near 3360 Å (*bottom panel*). The observed spectrum of HE 2327−5642 is shown as bold dots. The dashed curves in the *top and bottom panels* show the synthetic spectra with no carbon and nitrogen in the atmosphere. In the *middle panel*, the continuous curve corresponds to an isotope ratio of $^{12}C/^{13}C = 10$, while the dashed curves are synthetic spectra for $^{12}C/^{13}C = 3$ and 30.

also be convection-related (Cayrel et al. 2009), we cannot exclude there being a significant amount of ^{6}Li in HE 2327−5642. The departures from LTE cause only a minor increase in the derived lithium abundance, i.e, by 0.04 dex according to the calculations of Lind et al. (2009).

With an abundance of $\log\varepsilon(\mathrm{Li}) = 0.99$, HE 2327−5642 is located well below the lithium plateau for halo stars near the main-sequence turnoff, as expected for a red giant (Iben 1967).

Carbon was measured using CH lines in the regions 4310−4314 Å and 4362−4367 Å, which are almost free from intervening atomic lines (see Fig. 6, top panel). The C abundances obtained from these spectral bands are consistent with each other to within 0.03 dex (see Table 8, online material). The mean abundance is [C/Fe] = 0.13, which is similar to those of the giants with $T_{\rm eff} > 4800$ K from the sample of Cayrel et al. (2004).

We were able to use the only detectable ^{13}CH feature near 4211 Å to estimate the isotope ratio $^{12}C/^{13}C$. The best fit model for the region 4210.7−4212.2 Å including also two ^{12}CH features was achieved for $^{12}C/^{13}C = 10$ (Fig. 6, middle panel). However, because of the $S/N \simeq 100$ of the spectrum of HE 2327−5642 around 4211 Å, values of up to $^{12}C/^{13}C = 20$ were found to be possible.

The abundance of nitrogen could only be determined from the NH band at 3360 Å. In the literature, gf-values of the NH molecular lines calculated by Kurucz (1993) were subject to corrections based on analysis of the Solar spectrum around 3360 Å. Hill et al. (2002) apply a correction of −0.807 in $\log gf$ to all of the NH lines, and Hayek et al. (2009) −0.4 dex. We checked the rather crowded spectral region around 3360 Å in the Solar spectrum (Kurucz et al. 1984) and fitted it with gf-values of the NH lines that had been reduced by between −0.3 and −0.4 dex. With these corrections, we derived a relative abundance, [N/Fe], of between −0.30 and −0.20 (Fig. 6, bottom panel).

On the basis of its Li, C, and N abundances, HE 2327−5642 does not appear to be exceptional. Unfortunately, its oxygen abundance could not be determined from the available observed spectrum.

4.2. Sodium to titanium

In HE 2327−5642, the α-process elements Mg, Si, Ca, and Ti are enhanced relative to iron: [Mg/Fe] = 0.19, [Si/Fe] = 0.21, [Ca/Fe] = 0.28, and [Ti/Fe] = 0.10. This is consistent with the behavior of other metal-poor halo stars (see, e.g., Cayrel et al. 2004).

The determination of the abundances of Mg and Ca is based on NLTE line formation calculations for Mg I and Ca I-II, using the methods described by Zhao et al. (1998, Mg I) and Mashonkina et al. (2007a, Ca I-II). For both elements, the same scaling factor, $S_{\rm H} = 0.1$, was applied to the Steenbock & Holweger (1984) formula for calculations of the inelastic collisions with hydrogen atoms. Neutral Mg and Ca are minority species in the atmosphere of HE 2327−5642, and they are both subject to overionization caused by super-thermal ultraviolet radiation of non-local origin, resulting in a weakening of the Mg I and Ca I lines relative to their LTE strengths. The NLTE abundance corrections, $\Delta_{\rm NLTE} = \log\varepsilon_{\rm NLTE} - \log\varepsilon_{\rm LTE}$, are in the range 0.08–0.12 dex for the Mg I lines and between 0.17 and 0.29 dex for the Ca I lines (Table 8, online material).

The Si abundance was derived from the only detected line, Si I 3905 Å, assuming LTE. Based on the NLTE calculations for Si I presented by Shi et al. (2009), we estimated the NLTE abundance correction for this line to be positive and on the order of a few hundredths of a dex.

Titanium is observed in HE 2327−5642 for two ionization stages, and its abundance can be reliably determined. We obtained a difference in absolute LTE abundances of −0.07 dex between Ti I and Ti II. Assuming that the NLTE effects for Ti II are as small, as is the case for Fe II, and that they are of the same order for Ti I as they are for Fe I, we found that $\Delta\log\varepsilon(\mathrm{Ti\,I} - \mathrm{Ti\,II}) = 0.03$ dex.

HE 2327−5642 displays an underabundance of the odd-Z elements Na and Al relative to iron of [Na/Fe] = −0.60 and [Al/Fe] = −0.67. This is not exceptional for a metal-poor halo star. Sodium and aluminium were observed in HE 2327−5642 only in the resonance lines of their neutral species. The abundance determination was based on NLTE line formation for Na I and Al I, using the methods described by Mashonkina et al. (1993) and Baumüller & Gehren (1996). For both species, $S_{\rm H} = 0.1$ was adopted. The NLTE abundances derived from the Na I 5890/5896 Å lines are −0.39/ − 0.28 dex lower than the corresponding LTE values. In contrast, the NLTE abundance derived from Al I 3961 Å is 0.52 dex higher than the LTE value. It is worth noting that the calculated $\Delta_{\rm NLTE}$ of the Na lines agree within 0.05/0.02 dex with those given by Andrievsky et al. (2007) in their Table 2 for $T_{\rm eff}$, $\log g$, and W_λ values close to those of HE 2327−5642, while we found that $\Delta_{\rm NLTE}$ for Al I

is 0.25 dex lower than indicated by Andrievsky et al. (2008) in their Fig. 2 for similar stellar parameters. For the relative abundances in HE 2327−5642, we obtained an Al/Na ratio close to Solar ([Al/Na] = −0.07) and very low odd/even-Z ratios ([Na/Mg] = −0.79; [Al/Mg] = −0.86).

To determine the abundance of Sc, we employed four lines of the majority species Sc II. For each line, hyperfine structure splitting was taken into account, using the HFS data of McWilliam et al. (1995). Neglecting the HFS effect led to an overestimation of the Sc abundance of 0.08 dex for Sc II 4246 Å, the strongest line in the wavelength ranges covered by our spectra. We obtained [Sc/Fe] = −0.22, which is about 0.2 dex lower than the corresponding mean value for the cool halo giants studied by Cayrel et al. (2004). The difference can be at least partly explained by HFS not having been taken into account by Cayrel et al. (2004). NLTE calculations for Sc II in the Sun were performed by Zhang et al. (2008), with the result that the departures from LTE are small with negative NLTE abundance corrections of −0.06 to −0.03 dex.

4.3. Iron-group elements and Zn

We determined the abundance of six elements in this group. For two of them, Mn and Co, their energy levels are affected by considerable hyper-fine splitting, and HFS was explicitly taken into account in our spectrum synthesis calculations where HFS data were available (see Table 8 online for references).

For Mn, we measured 0.36 dex lower abundances from the Mn I resonance lines at ∼ 4030 Å than from the Mn I subordinate line at 4041 Å in HE 2327−5642. A similar effect was found for the Cr I lines: two lines originating from the ground state, 4254 Å and 4274 Å, corresponded to 0.26 and 0.32 dex lower abundances than the mean of the other chromium lines. Our results are consistent with the findings of Johnson (2002) and later studies. The Mn abundance derived from the Mn I lines may be underestimated because of departures from LTE. Bergemann & Gehren (2008) predict $\Delta_{\rm NLTE}$ = 0.37 − 0.41 dex for the Mn I resonance triplet in the model 5000/4.0/−3, and 0.5 dex for Mn I 4041 Å. Usually, the NLTE effects become more pronounced with decreasing $\log g$. However, it is unclear whether $\Delta_{\rm NLTE}$ will vary with surface gravity in similar ways for the Mn I resonance triplet and Mn I 4041 Å. Therefore, the abundances derived from the Mn I resonance lines were not taken into account in calculating the mean presented in Table 5.

We fortunately detected lines of Mn II, the majority species of Mn, which is hardly expected to be affected by departures from LTE, according to the results of Bergemann & Gehren (2007). We note that the relative LTE abundances [Mn I (4041 Å)/Fe I] and [Mn II/Fe II] in HE 2327−5642 are consistent with each other to within 0.01 dex. Though HFS was not taken into account for the Mn I 4041 Å line, its effect on the abundance is expected to be small, as the line is very weak (W_λ = 11 mÅ). We measure for HE 2327−5642 an underabundance of Cr and Mn very similar to that of the comparison sample (Cayrel et al. 2004).

HE 2327−5642 is also deficient in V and Ni relative to iron and Solar ratios. Information about V abundances in very metal-poor stars is scarce in the literature, probably due to difficulties in detecting the vanadium lines. We used four lines of V II located in the blue spectral range, where severe blending effects are present even in very metal-poor stars. Paper II found V/Fe ratios close to Solar for the sample covering a [Fe/H] range from −1.5 to −3. However, they noted that the V abundances are based on quite weak features and hence are susceptible to overestimation due to unresolved blends. For Ni, we used eight well observed and unblended lines of Ni I. The large scatter in the abundances obtained may be partly caused by our using four different sources for the gf-values (see Table 8 online for references). For example, the mean abundance derived from two lines using the gf-values of Fuhr et al. (1988) is 0.21 dex higher than the abundances measured from three lines employing the gf-values of Blackwell et al. (1989).

For the cobalt and zinc abundances of HE 2327−5642, we obtained values close to the Solar ratios with respect to iron, i.e., [Co I/Fe I] = −0.07 and [Zn I/Fe I] = 0.09. Using $\Delta_{\rm NLTE}$(Zn I 4810 Å) = +0.05 from the NLTE calculations of Takeda et al. (2005), and assuming similar departures from LTE for Zn I 4722 Å, we calculated a NLTE abundance ratio of [Zn/Fe] = 0.04. Cayrel et al. (2004) found that [Co/Fe] and [Zn/Fe] increase with decreasing metallicity, and measured [Co/Fe] ≃ 0.25 and [Zn/Fe] ≃ 0.2 for stars with [Fe/H] close to −2.8 (see their Fig. 12). We note that Cayrel et al. (2004) neglected HFS of the used lines of Co I, thus they probably overestimated the Co abundances. According to our estimate for Co I 4121 Å in the atmospheric model 5050/2.34/−2.78, ignoring HFS makes a difference in abundance of +0.09 dex.

4.4. Heavy elements

In the "snapshot" spectra of HE 2327−5642, Barklem et al. (2005) detected only six heavy elements beyond strontium. Owing to the higher quality and broader wavelength coverage of the spectra used in this study, we detected 23 elements in the nuclear charge range between Z = 38 and 90. We were unsuccessful in obtaining abundances for Ru, Rh, and U. The Ru I 3436, 3728 Å and Rh I 3434, 3692 Å lines are very weak and therefore could not be detected in our spectra. We marginally detected the U II 3859.57 Å line in our spectra of HE 2327−5642; however, the S/N is not high enough to derive a reliable abundance.

4.4.1. NLTE effects

For five species, Sr II, Zr II, Ba II, Pr II, and Eu II, we performed NLTE calculations using the methods described in our earlier studies (Belyakova & Mashonkina 1997; Velichko et al. 2010; Mashonkina et al. 1999, 2009; Mashonkina & Gehren 2000) and determined the NLTE element abundances. They are presented in Table 8 (online material).

Our NLTE calculations for HE 2327−5642 showed that the Sr II and Ba II resonance lines are stronger than in the LTE case, resulting in negative NLTE abundance corrections of −0.15 dex and −0.09 dex, respectively. The subordinate lines of Ba II exhibit a different behavior: the weakest line at 5853 Å is weaker, while the other two lines, at 6141 and 6496 Å, are stronger relative to their values for LTE.

In contrast to Sr II and Ba II, the term structure of the other NLTE species is produced by multiple electronic configurations and consists of hundreds and thousands of energy levels. For each of these species, enhanced photoexcitation from the ground state leads to overpopulation of the excited levels in the line formation layers, resulting in a weakening of the lines. We calculated positive NLTE abundance corrections for the lines of Zr II, Pr II, and Eu II, finding values close to +0.1 dex. All the elements beyond barium are observed in the lines of their majority species, with term structures as complicated as that for Eu II, so the departures from LTE are expected to be similar to those for Eu II. This

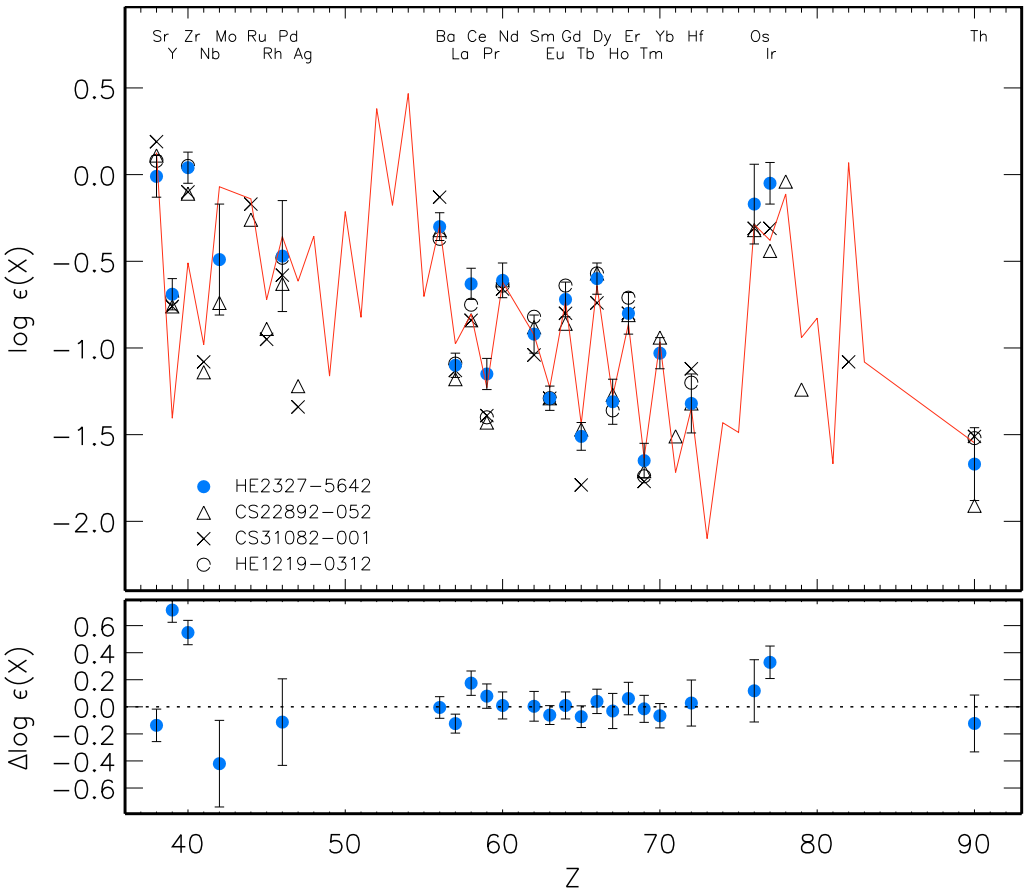

Fig. 7. The heavy-element abundance pattern of HE 2327−5642 (filled circles) compared to the Solar System *r*-process (SSr) abundance pattern (continuous curve) scaled to match Ba–Hf. For comparison, the heavy element abundances of the benchmark r-II stars CS 22892-052 (open triangles), CS 31082-001 (crosses), and HE 1219-0312 (open circles) are shown. They have been normalized to the value derived for $\log \varepsilon_{\rm Eu}$ in HE 2327−5642. The bottom panel displays the difference between HE 2327−5642 and SSr defined as $\Delta \log \varepsilon(X) = \log \varepsilon_{\rm HE\,2327-5642}(X) - \log \varepsilon_{\rm SSr}(X)$.

is largely true also for osmium and iridium detected in the lines of their neutrals, Os I and Ir I, which have relatively high ionization energies of 8.44 and 8.97 eV, respectively. Fortunately, the abundance *ratios* among heavy elements are probably only weakly affected by departures from LTE. For consistency, we used in this study the abundances of the heavy elements beyond strontium as determined based on the LTE assumption. They are presented in Table 5 and Fig. 7.

We now explore the abundance patterns of elements in the three *r*-process peaks.

4.4.2. The light trans-iron elements

Five elements with $38 \le Z \le 46$ were measured in the region of the first peak. The only molybdenum line in the visible spectrum, Mo I 3864 Å, can be used to determine the element abundance of cool stars. In HE 2327−5642, this line is nearly free of blends, but it is weak: the central depth of the line is only ∼2% of the continuum. With $S/N \simeq 50$ of the observed spectrum within this wavelength region, the uncertainty in the derived Mo abundance was estimated to be 0.3 dex.

A similar uncertainty is expected for palladium, which was detected in a single line, Pd I 3404 Å. In HE 2327−5642, this line is free of blends and is stronger than that of Mo I 3864 Å, but it is located in a spectral range where the S/N is only 20 to 25.

Strontium is observed in HE 2327−5642 in two strong resonance lines, Sr II 4077 and 4215 Å. Both lines are affected by HFS of the odd isotope ^{87}Sr. The synthetic spectrum was calculated with the ^{87}Sr fraction of 0.22 corresponding to a pure *r*-process production of strontium (Arlandini et al. 1999, stellar model).

4.4.3. The second *r*-process peak elements

With 15 elements measured in the Ba–Hf range (see Fig. 8 for holmium and hafnium), the second *r*-process peak is the most tightly constrained among the three peaks.

The barium abundance given in Table 5 was determined from the three subordinate lines, Ba II 5853, 6141, and 6497 Å, which are almost free of HFS effects. According to our estimate for Ba II 6497 Å, neglecting HFS makes a difference in abundance of no more than 0.01 dex. In contrast, the Ba II 4554 Å resonance line is strongly affected by HFS. The even isotopes are unaffected by HFS, while the odd isotopes exhibit significant HFS, and thus the element abundance derived from this line depends on the Ba isotope mixture adopted in the calculations. Since the odd isotopes ^{135}Ba and ^{137}Ba have very similar HFS, the abundance is essentially dependent on the total fractional abundance of these odd isotopes, $f_{\rm odd}$. For example, using the Solar Ba isotope mixture with $f_{\rm odd} = 0.18$, we inferred an abundance that was 0.34 dex higher from Ba II 4554 Å than the mean abundance of the subordinate lines. In the LTE calculations, the difference was reduced by 0.20 dex when we adopted a pure *r*-process Ba isotope mixture with $f_{\rm odd} = 0.46$, as predicted by

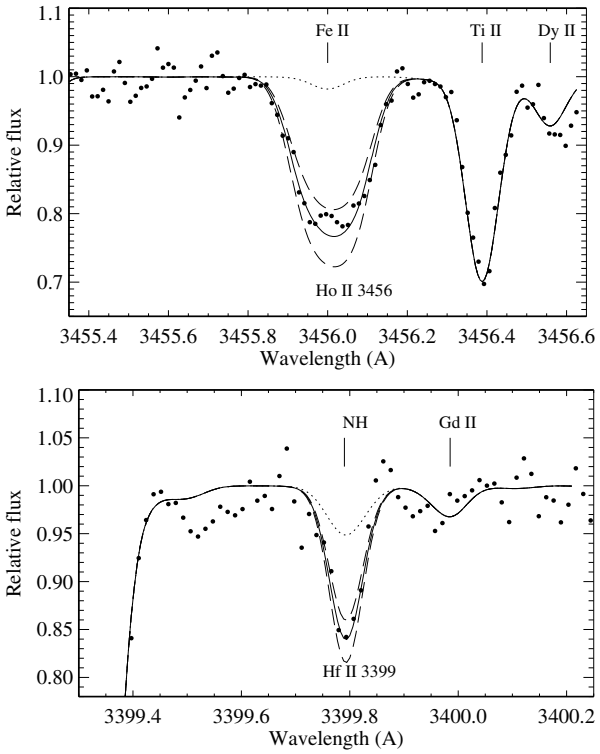

Fig. 8. The best fits (continuous curve) of Ho II 3456 Å (*top panel*) and Hf II 3399 Å (*bottom panel*) in the observed spectrum of HE 2327−5642 (bold dots). The dashed curves show the effect of a 0.1 dex variation in the abundance on the synthetic spectrum. The dotted curves show the synthetic spectrum with no holmium and hafnium in the atmosphere.

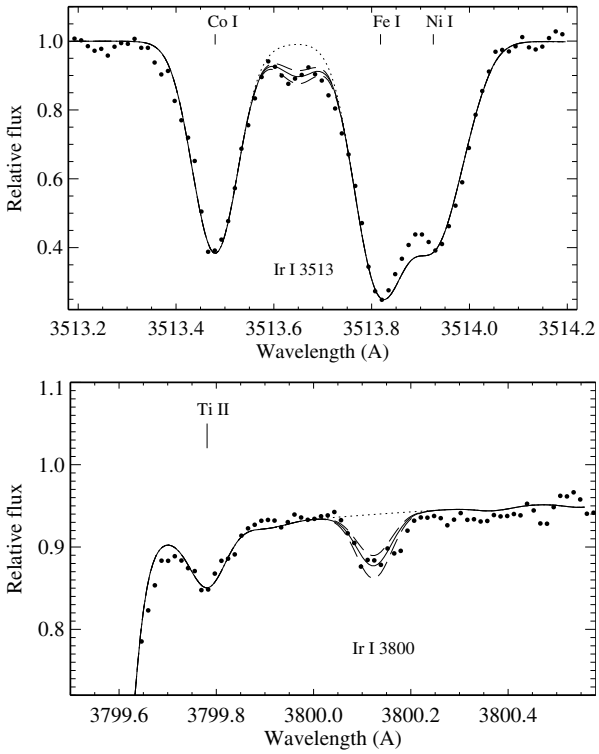

Fig. 9. The same as in Fig. 8, but for Ir I 3513 and 3800 Å.

Arlandini et al. (1999, stellar model). The remaining discrepancy between the resonance and subordinate lines was largely removed by NLTE calculations. Thus, our analysis of HFS affecting the Ba II 4554 Å resonance line suggests a pure *r*-process origin of barium in HE 2327−5642.

The lines of Eu II and Yb II detected in HE 2327−5642 consist of multiple IS and HFS components. To derive the total abundance of the given element, we adopted in our calculations a pure *r*-process isotope mixture from the predictions of Arlandini et al. (1999, stellar model): ^{151}Eu : ^{153}Eu = 39:61 and ^{171}Yb : ^{172}Yb : ^{173}Yb : ^{174}Yb : ^{176}Yb = 18.3 : 22.7 : 18.9 : 23.8 : 16.3. All the lines of Nd II and Sm II observed in HE 2327−5642 are rather weak, and are treated as single lines.

Only one hafnium line can be measured in HE 2327−5642. The observed feature is attributed to a combination of the Hf II 3399.79 Å and NH 3399.79 Å molecular line. Using $\log gf = -1.358$ taken from Kurucz (1993) and reduced by −0.3 dex, and the nitrogen abundance $\log \varepsilon_{\rm N} = 4.78$, the molecular line contributes approximately 45 % to the 3399 Å blend (Fig. 8). Ignoring the molecular contaminant completely leads to a 0.17 dex higher hafnium abundance. We therefore estimate the uncertainty in the Hf abundance obtained to be 0.15 dex.

4.4.4. The heaviest elements

The third peak and actinides were probed for three elements, osmium, iridium, and thorium. The abundance of osmium was determined from a single line, Os I 4260 Å. The line is weak, with a center line depth of 2.5% in the continuum flux, and is nearly free of blends. Because of the high $S/N \simeq 100$ of the observed spectrum, the uncertainty in the derived osmium abundance was estimated as 0.2 dex.

Two iridium lines, Ir I 3513 and 3800 Å, were clearly detected in HE 2327−5642 (Fig. 9). The theoretical profiles were calculated by taking HFS effects into account and iridium isotope abundance ratio ^{191}Ir:^{193}Ir = 37 : 63, which is obtained to be the same in the matter for the Solar System (Lodders 2003) and the matter produced by the *r*-process (Arlandini et al. 1999). The Ir I 3800 Å line was measured in two observed spectra, BLUE390 and 437BLUE, (Table 2) and seems reasonably to be reliable. With its equivalent width of 5.8 mÅ and $S/N \simeq 100$ of the observed spectrum, the uncertainty in the derived iridium abundance was estimated to be 0.08 dex. The Ir I 3513 Å line served as a verification that it agrees with the other line. The blend at 3513.6 Å is well reproduced by assuming the value of $\log \varepsilon_{\rm Ir} = -0.05$ found from Ir I 3800 Å, as shown in Fig. 9.

The radioactive element thorium was clearly detected in HE 2327−5642 in the Th II 4019 Å line (Fig. 10), but proved rather challenging to incorporate into the determination of the stellar age of HE 2327−5642. Unhappily, the observed spectrum around Th II 4019 Å has low signal-to-noise ratio ($S/N \simeq 50$), and the uncertainty in the derived thorium abundance was estimated to be 0.2 dex.

4.5. Error budget

We performed a detailed error analysis of HE 2327−5642, to estimate the uncertainties in the abundance measurements for the heavy elements beyond the iron group. Stochastic errors ($\sigma_{\rm obs}$) caused by random uncertainties in the continuum placement, line profile fitting, and gf-values, are represented by a dispersion in the measurements of multiple lines around the mean ($\sigma_{\log \varepsilon}$), as given in Table 5 when $N \geq 2$ lines of an element are observed. Observational errors in the species with a single line used in

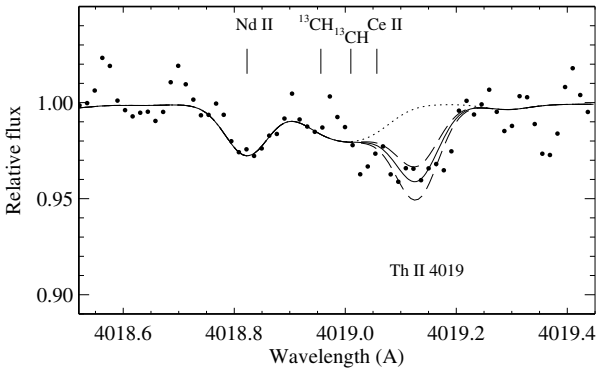

Fig. 10. The same as in Fig. 8, but for Th II 4019 Å.

abundance analysis were discussed in Sect. 4.4. Systematic uncertainties include those that exist in the adopted stellar parameters, in the used hydrostatic model atmospheres, and in the LTE line formation calculations. As argued in Sect. 4.4, the latter is not expected to influence the abundance pattern of the elements in the range from La to Th.

It is difficult to estimate the uncertainty introduced by using the 1D model atmosphere. The elements in the La–Th range, for example, are observed in the lines of their majority species. The detected lines arise from either the ground or low-excitation levels, and most of them are relatively weak, i.e., $W_\lambda < 30$ mÅ. This means that they all are formed in the same atmospheric layers. It would therefore be rather unexpected for there to be significantly different 3D effects for individual elements in the La–Th range. This is different from the case of the elements in the Sr–Pd range, Ba, and Yb, which are observed in either the strong lines (e.g. Sr II 4215 Å, Ba II 6141 Å, Yb II 3694 Å) or the lines of the minority species Mo I and Pd I. Both NLTE and 3D effects may have a strong influence on their derived abundance. Hence, we examined here only those uncertainties linked to our choice of stellar parameters. These were estimated by varying $T_{\rm eff}$ by −70 K, $\log g$ by −0.1 dex, and ξ by −0.1 km s^{-1} in the stellar atmosphere model.

Table 6 summarizes the various sources of uncertainties. The quantity $\Delta(T, g, \xi)$ listed in Col. 5 is the total impact of varying each of the three parameters, computed as the quadratic sum of Cols. 2−4. The total uncertainty $\sigma_{\rm tot}$ (Col. 7) in the absolute abundance of each element is computed by the quadratic sum of the stochastic ($\sigma_{\rm obs}$) and systematic ($\Delta(T, g, \xi)$) errors.

5. Comparison to other r-II stars and Solar *r*-process abundances

The abundance pattern of the neutron-capture elements in the range from Sr to Os in HE 2327−5642 is very similar to that of other well-studied r-II stars. Figure 7 shows comparisons with CS 22892-052 (Sneden et al. 2003), CS 31082-001 (Hill et al. 2002; Plez et al. 2004), and HE 1219-0312 (Hayek et al. 2009). For example, the dispersion about the mean of the quantities ($\log \varepsilon_{\rm HE\,2327-5642} - \log \varepsilon_{\rm CS\,22892-052}$) amounts to 0.10 dex, which is at the level of 1σ error bars in the abundance determinations of the individual elements.

Iridium in HE 2327−5642 seems to be overabundant with respect to CS 22892-052 and CS 31082-001. Roederer et al. (2009) compiled and/or revised the neutron-capture element abundances for a sample of *r*-process rich stars including CS 22892-052 and CS 31082-001, and they obtained a mean iridium to europium ratio of log(Ir/Eu) = 0.90 ± 0.09 for 15 stars. For

Table 6. Error budget for neutron-capture elements in HE 2327−5642.

El.	ΔT	$\Delta \log g$	$\Delta\xi$	Δ	$\sigma_{\rm obs}$	$\sigma_{\rm tot}$
	−70 K	−0.1 dex	−0.1 km s^{-1}	(T, g, ξ)		
(1)	(2)	(3)	(4)	(5)	(6)	(7)
Sr II	−0.08	−0.01	0.09	0.12	0.00	0.12
Y II	−0.05	−0.03	0.02	0.06	0.06	0.09
Zr II	−0.06	−0.03	0.02	0.07	0.05	0.09
Mo I	−0.10	<0.01	<0.01	0.10	0.3	0.32
Pd I	−0.10	<0.01	<0.01	0.10	0.3	0.32
Ba II	−0.06	−0.03	0.03	0.07	0.03	0.08
La II	−0.06	−0.03	<0.01	0.07	0.02	0.07
Ce II	−0.06	−0.03	<0.01	0.07	0.06	0.09
Pr II	−0.06	−0.03	<0.01	0.07	0.06	0.09
Nd II	−0.06	−0.03	0.01	0.07	0.08	0.10
Sm II	−0.06	−0.03	<0.01	0.07	0.09	0.11
Eu II	−0.06	−0.03	0.01	0.07	0.02	0.07
Gd II	−0.06	−0.03	0.01	0.07	0.07	0.10
Tb II	−0.07	−0.03	0.01	0.08	0.03	0.08
Dy II	−0.06	−0.03	0.03	0.07	0.06	0.09
Ho II	−0.07	−0.03	<0.01	0.08	0.10	0.13
Er II	−0.07	−0.03	<0.01	0.08	0.09	0.12
Tm II	−0.06	−0.03	0.01	0.07	0.08	0.10
Yb II	−0.04	−0.03	0.07	0.09	0.02	0.09
Hf II	−0.07	−0.03	0.01	0.08	0.15	0.17
Os I	−0.11	<0.01	<0.01	0.11	0.2	0.23
Ir I	−0.09	−0.01	<0.01	0.09	0.08	0.12
Th II	−0.07	−0.03	<0.01	0.08	0.2	0.21

HE 2327−5642, we derived log(Ir/Eu) = 1.24. We investigated the possible sources of the difference between our analysis and that of Roederer et al. (2009), identifying one that could at least partly explain it. The iridium abundances of Roederer et al. (2009) were underestimated by approximately 0.2 dex because they used the partition functions of Ir II implemented in the MOOG code (C. Sneden, private communication), which are about a factor of two lower than that we used in our study. We compared the partition functions thoroughly and are satisfied that our new data, which are based on the highest quality energy level data available, are more accurate. In all other relevant respects (i.e., gf-values, HFS data, ionization potential of Ir I), our data and methods and those of Roederer et al. (2009) are identical. The difference in the codes used for the abundance determination cannot play a role only for iridium, leaving all the other determinations unaffected. Hence, we are left with a discrepancy of 0.14 dex in log(Ir/Eu) between HE 2327−5642 and the stellar sample of Roederer et al. (2009). However, to draw any firm conclusion at this point, the abundance determinations have to be confirmed using more accurate measurements and the latest detections of the third *r*-process peak elements.

In Fig. 7, we also plot the Solar *r*-process residuals. The decomposition of the *s*- and *r*-process contributions is based on the meteoritic abundances of Lodders et al. (2009) and the *s*-process abundances of Arlandini et al. (1999, stellar model). The absolute *s*-process abundances were obtained by Arlandini et al. (1999) by normalizing the calculated *s*-process abundances to the Solar abundance of the pure *s*-process isotope ^{150}Sm taken from Anders & Grevesse (1989). The difference in the Sm abundance between Anders & Grevesse (1989) and Lodders et al. (2009) was taken into account. Hereafter, the Solar *r*-residuals are referred to as the Solar system *r*-process (SSr) abundance pattern.

The elements in the range from Ba to Hf in HE 2327−5642 were found to match the scaled Solar *r*-process pattern very well, with a dispersion of 0.07 dex about the mean of the differences

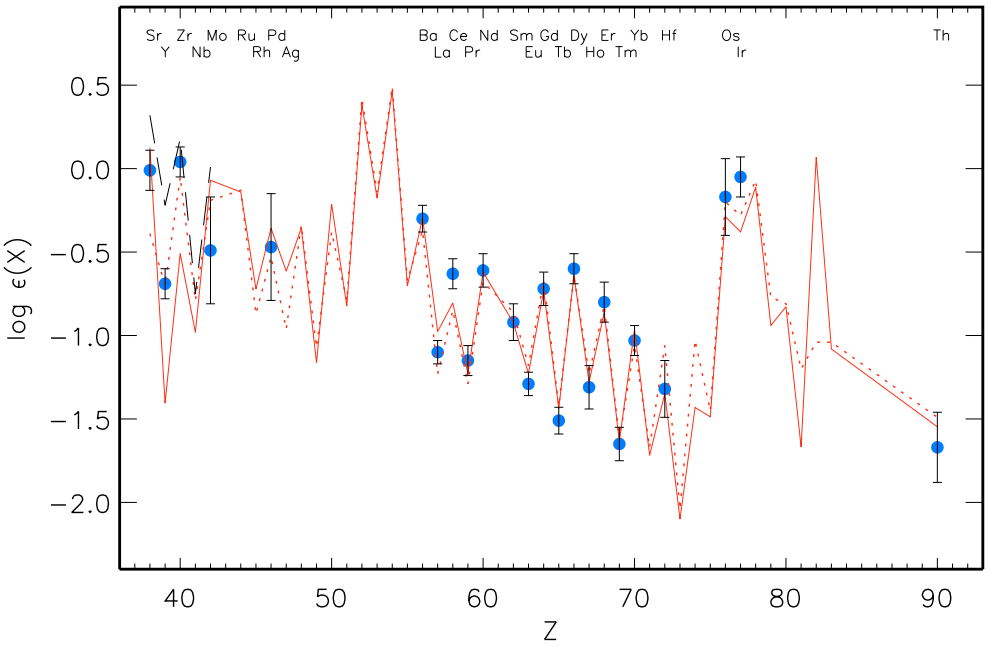

Fig. 11. The heavy-element abundance pattern of HE 2327−5642 (filled circles) compared to the *r*-residuals calculated with various Solar total abundances and *s*-process abundances. Continuous and dotted curves correspond to the predicted *s*-process abundances of Arlandini et al. (1999, stellar model) and the Solar total abundances from Lodders et al. (2009) and Asplund et al. (2009), respectively. The dashed curve (only Sr−Mo) corresponds to the *s*-process abundances of Travaglio et al. (2004) and the Solar total abundances of Lodders et al. (2009). Each *r*-process abundance pattern was scaled to match the Ba–Hf in HE 2327−5642.

($\log \varepsilon_{\rm HE\,2327-5642} - \log \varepsilon_{\rm SSr}$). This is in line with earlier results obtained for other *r*-process rich stars, e.g., CS 22892-052 (Sneden et al. 2003), CS 31082-001 (Hill et al. 2002), HD 221170 (Ivans et al. 2006), CS 29491-069, and HE 1219-0312 (Hayek et al. 2009), and provides additional evidence of universal production ratio of these elements during the Galactic history. It is worth noting that the use of the partition function of Ho II from Bord & Cowley (2002) improves the comparison with the scaled Solar *r*-process for holmium.

For the lighter elements in HE 2327−5642, the difference $\Delta \log \varepsilon(X) = \log \varepsilon_{\rm obs}(X) - \log \varepsilon_{\rm SSr}(X)$ is indicative of a large spread of the data, between −0.4 dex (Mo) and +0.7 dex (Y). In the following, we show that at least a major fraction of the departures from the Solar *r*-process found for the light trans-iron elements is likely to be due to inaccurate Solar *r*-residuals.

For a given element, the *r*-residual is obtained by subtracting theoretical *s*-process yields from the observed total Solar abundance. We consider, for instance, the *s*-process abundances from Arlandini et al. (1999, stellar model) and use the Solar total abundances from two different sources, Lodders et al. (2009, meteoritic) and Asplund et al. (2009, photospheric). The 0.02 dex increase in the yttrium abundance as one changes from Lodders et al. (2009) to the Asplund et al. (2009) data leads to a 0.65 dex increase in the *r*-residual. A notable difference between two sets of the Solar *r*-process abundances was found for all elements with dominant *s*-process contribution to their Solar abundances, for example, −0.58 dex for Sr, −0.40 dex for Zr, and −0.31 dex for La (see Fig. 11). This is because the calculation of the *r*-residuals involves the subtraction of a large number from another large number, so that any small variations of one of them leads to a dramatic change in the difference.

Significant uncertainties in the *r*-residual are also caused by differences between *s*-process calculations. For example, Arlandini et al. (1999) obtained the *s*-process abundance distribution by performing a best-fit to the Solar *main* *s*-component using stellar AGB models of 1.5 $M_\odot$ and 3 $M_\odot$ with half-Solar metallicity. Travaglio et al. (1999, 2004) calculated the *s*-process contribution to the Solar abundances by integrating of the *s*-process yields of different generations of AGB stars, i.e., considering the whole range of Galactic metallicities. In both studies, very similar results were found for Ba and Eu; however, Travaglio et al. (2004) predicted lower *s*-process abundances for the elements in the Sr−Mo range. In consequence, their Solar *r*-residuals were significantly increased, as shown in Fig. 11. From this discussion, it is clear that no solid conclusion can be drawn about any departures from the scaled Solar *r*-process pattern in the Sr–Pd region for r-II stars.

Observations of metal-poor halo stars appear to infer a distinct production mechanism for the light trans-iron (Sr–Zr) and heavy elements beyond Ba in the early Galaxy (Aoki et al. 2005; François et al. 2007; Mashonkina et al. 2007b). We have chosen strontium and europium as representative elements of the first and second neutron-capture element peaks and inspected the Sr/Eu abundance ratios in a pre-selected sample of halo stars with a dominant contribution of the *r*-process to the production of heavy elements beyond Ba, i.e., with [Ba/Eu] ≤ -0.4. The stars are separable into three groups, depending on the observed europium enhancement. Nine r-II stars ([Eu/Fe] > 1.0) were taken from Hill et al. (2002); Sneden et al. (2003); Christlieb et al. (2004); Honda et al. (2004); Barklem et al. (2005); François et al. (2007); Lai et al. (2008), and Hayek et al. (2009), 32 r-I stars ($0.2 \leq$ [Eu/Fe] < 1) from Cowan et al. (2002); Honda et al. (2004); Barklem et al. (2005); Ivans et al. (2006); François et al. (2007); Mashonkina et al. (2007b); Lai et al. (2008), and Hayek et al. (2009), and 12 stars with [Eu/Fe] ≤ 0.06 (hereafter Eu-poor stars) from Honda et al. (2004, 2006, 2007); Barklem et al. (2005), and François et al. (2007).

As expected, all stars within each group have very similar Ba/Eu abundance ratios, as shown in the bottom panel of Fig. 12, where mean Ba/Eu ratios of log(Ba/Eu) = 1.05 ± 0.10

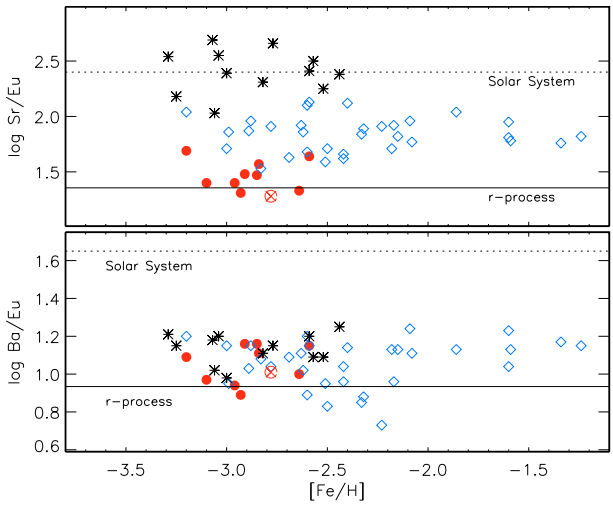

Fig. 12. The Sr/Eu (*top panel*) and Ba/Eu (*bottom panel*) abundance ratios in r-II (filled circles), r-I (open rombs), and Eu-poor (asterisks) stars (for the sources of the data, see text). HE 2327−5642 is shown by a crossed open circle. The solid and dotted lines indicate the pure *r*-process and Solar system ratios, respectively.

(r-II stars), 1.06 ± 0.13 (r-I stars), and 1.14 ± 0.08 (Eu-poor stars). We note that $\log(\mathrm{Ba/Eu})_r = 0.93$ for a pure *r*-process production of heavy elements (Arlandini et al. 1999). This suggests that only a small number of *s*-nuclei (including those of strontium) existed in the matter out of which these stars formed. The Sr/Eu abundance ratios indicate a clear separation between each of these three groups (Fig. 12). We note that the Zr/Eu ratios exhibit very similar behavior. The mean Zr/Eu abundance ratios are $\log(\mathrm{Zr/Eu}) = 1.42 \pm 0.19$ (r-II stars), 1.75 ± 0.15 (r-I stars), and 2.30 ± 0.20 (Eu-poor stars). HE 2327−5642, having $\log(\mathrm{Ba/Eu}) = 1.01$, $\log(\mathrm{Sr/Eu}) = 1.28$ (crossed circle in Fig. 12), and $\log(\mathrm{Zr/Eu}) = 1.33$, clearly belongs to the group of r-II stars.

From Figs. 7 and 12, it is clear that the first and second *r*-process peak elements in the r-II stars are of common origin. However, the origin of the first neutron-capture peak elements in the r-I and Eu-poor stars remains unclear, despite being the subject of a number of studies (Truran et al. 2002; Travaglio et al. 2004; Farouqi et al. 2009).

6. Age determination

The detection of thorium permits a nucleo-chronometric age estimation of HE 2327−5642 by comparing the observed Th-to-stable neutron-capture element-abundance ratios with the corresponding initial values at the time when the star was born, $\log(\mathrm{Th}/X)_0$:

$$\tau = 46.7\,\mathrm{Gyr}\,\left[\log(\mathrm{Th}/X)_0 - \log(\mathrm{Th}/X)_{\mathrm{obs}}\right].$$

Because of the uncertainty in the thorium abundance of 0.2 dex, which translates into an age uncertainty of 9.3 Gyr, a precise age estimation is not possible. Nevertheless, we investigated how the results depend on the adopted values of $\log(\mathrm{Th}/X)_0$, and which Th/*X* pairs are possibly reliable chronometers. We assumed that thorium was produced with the lighter elements in the range between Ba and Hf.

We first determined the age of the star using the initial abundance ratios from the dynamical network calculations of Farouqi et al. (2008). They considered a core-collapse supernova (SN II) with an adiabatically expanding high-entropy wind (HEW) as the astrophysical environment for the *r*-process. In the HEW scenario, the total nucleosynthetic yield is the sum of SN ejecta with multiple components in different entropy ranges. Farouqi et al. (2008) found that heavy elements beyond $Z \simeq 52$ are produced in the highest entropy ($S > 150$) zones in the so-called "main" *r*-process. The HEW model production ratios, $\mathrm{PR} = \log(\mathrm{Th}/X)_0$, as given by Hayek et al. (2009), and the calculated ages for multiple Th/*X* pairs (where *X* is one of the elements in the Ba–Ir range for which we determined an abundance) are listed in Table 7.

The age uncertainties introduced by the measurement uncertainties are listed in the column "Error". They were calculated as $\sigma_\tau = 46.7\,\sqrt{\sigma^2_{\mathrm{obs}}(X) + \sigma^2_{\mathrm{obs}}(\mathrm{Th})}\,\mathrm{Gyr}$, where σ_{obs} is taken from Table 6. Variations in the stellar parameters T_{eff} and $\log g$ yielded an uncertainty of 1.5 Gyr in the final age. It can be seen that individual pairs indicate a large spread in stellar age. The mean value is $\tau = 15.1 \pm 7.4$ Gyr. As noted by Hayek et al. (2009), the estimate for hafnium in the HEW model is rather uncertain due to problems with the nuclear data. Neglecting hafnium and also osmium, because of less reliable stellar abundance, yields $\tau = 13.3 \pm 6.2$ Gyr, which agrees well with the expected age of an extremely metal-poor star that formed in the early Galaxy. We note that the cosmic age derived from the results of the *Wilkinson Microwave Anisotropy Probe (WMAP)* experiment is 13.7 ± 0.2 Gyr (Spergel et al. 2003).

For an additional estimate of the age of HE 2327−5642, we employed the Solar *r*-residual ratios $(\mathrm{Th}/X)_0$ for the elements for which the *r*-process fraction exceeds 70% (columns SSr in Table 7). Since these are measured values, they depend only weakly on theoretical predictions and their associated nuclear physics uncertainties. Since the Sun is approximately 4.5 Gyr old, the corresponding correction accounting for the thorium radioactive decay was introduced to the Solar current thorium abundance. The resulting mean age of HE 2327−5642, $\tau = 7.4 \pm 5.5$ Gyr, calculated using all stable elements from Sm to Ir seems low for a halo star. If we neglect the estimate based on Th/Ir, which is clearly an outlier (i.e., $\tau = 21.0$ Gyr), we obtain an even lower stellar age of $\tau = 5.9 \pm 2.8$ Gyr.

We note that the stochastic error in the stellar age based on the HEW model predictions is large compared to that for the Solar *r*-residual ratios. This is probably caused by the uncertainty in the theoretical yields for individual elements.

7. Conclusions

The high-quality VLT/UVES spectra of HE 2327−5642 has enabled us to determine accurate abundances for 40 elements, including 23 elements in the nuclear charge range $Z = 38$–90. We have confirmed that HE 2327−5642 is strongly *r*-process enhanced, having $[r/\mathrm{Fe}] = 0.99 \pm 0.03$ where *r* denotes the average of the abundances of seven elements (i.e., Eu, Gd, Tb, Dy, Ho, Er, and Tm), where there is an *r*-process contribution to the Solar system matter of more than 85 % according to the *r*-residuals of Arlandini et al. (1999). We have found that HE 2327−5642 and three benchmark r-II stars, i.e., CS 22892-052 (Sneden et al. 2003), CS 31082-001 (Hill et al. 2002), and HE 1219-0312 (Hayek et al. 2009) have very similar abundance patterns of the elements in the range from Sr to Os. Hence, HE 2327−5642 is a member of the small sample of currently known r-II stars.

The elements in the range from Ba to Hf in HE 2327−5642 match the scaled Solar *r*-process pattern very well. We have shown that the Solar *r*-residuals for the first *r*-process peak

Table 7. Logarithmic production ratios (PR) for the HEW model and Solar System *r*-process (SSr) and corresponding radioactive decay ages in HE 2327−5642.

Element pair	Stellar ratio	HEW $S = 10 \ldots 300$ PR	HEW age, Gyr	Error, Gyr	SSr PR	SSr age, Gyr
Th/Ba	−1.37	−0.96	19.1	9.4		
Th/La	−0.57	−0.22	16.3	9.4		
Th/Ce	−1.04	−0.62	19.6	9.8		
Th/Pr	−0.52	−0.20	14.9	9.8		
Th/Nd	−1.06	−0.87	8.9	10.0		
Th/Sm	−0.75	−0.71	1.9	10.2	−0.62	6.1
Th/Eu	−0.38	−0.32	2.8	9.4	−0.32	2.8
Th/Gd	−0.95	−0.73	10.3	9.9	−0.82	6.1
Th/Tb	−0.16				−0.11	2.3
Th/Dy	−1.07	−0.69	17.7	9.8	−0.91	7.5
Th/Ho	−0.36	0.04	18.7	10.4	−0.27	4.2
Th/Er	−0.87	−0.48	18.2	10.2	−0.69	8.4
Th/Tm	−0.02	0.22	11.2	10.0	0.08	4.7
Th/Hf	−0.35	0.20	25.7	11.7		
Th/Os	−1.50	−0.93	26.6	13.2	−1.26	11.2
Th/Ir	−1.62			10.1	−1.17	21.0
mean(Ba–Ir)			15.1 ± 7.4			7.4 ± 5.5
final			13.3 ± 6.2 (Ba–Tm)			5.9 ± 2.8 (Sm–Os)

elements are rather uncertain. They may vary by as much as 0.5 dex or even more, depending on the adopted Solar total abundances and *s*-process fractions. Therefore, no firm conclusion can be drawn about any relation between the light trans-iron elements in r-II stars and the Solar *r*-process.

We have found a clear distinction in Sr/Eu abundance ratios between the halo stars of different europium enhancement. We have proposed using the [Sr/Eu] ratio in addition to [Eu/Fe] to separate the strongly *r*-process enhanced (r-II) stars from the other halo stars that have experienced a dominant contribution of the *r*-process to heavy element production. The r-II stars, whose stellar matter presumably has experienced a single nucleosynthesis event, have [Eu/Fe] $> 1 \pm 0.1$, [Ba/Eu] $= -0.60 \pm 0.10$, and a low Sr/Eu abundance ratio of [Sr/Eu] $= -0.92 \pm 0.13$. Stars with very similar Ba/Eu ratios have two times (0.36 dex) higher Sr/Eu ratios if their Eu/Fe ratio is in the range $1.0 >$ [Eu/Fe] > 0.2 (i.e., r-I stars), and nearly an order of magnitude (0.93 dex) higher Sr/Eu ratios if [Eu/Fe] < 0 (Eu-poor stars). The origin of the first neutron-capture peak elements in the r-I stars and Eu-poor stars remains unclear, and additional theoretical studies are needed to elucidate this problem.

Only two elements, Os and Ir, of the third *r*-process peak were detected in HE 2327−5642. Iridium appears to be overabundant compared to the Ir abundance determined in other *r*-process enhanced stars. However, due to the uncertainty in the Ir abundance, we have been unable to draw a firm conclusion.

The detection of thorium permitted an estimate of the radioactive decay age of HE 2327−5642, although the age uncertainty of 9.3 Gyr introduced by the uncertainty in the thorium abundance is rather large. Employing multiple Th/*X* chronometers and initial production ratios based on the Solar *r*-residuals, an age of 5.9 ± 2.8 Gyr was obtained from nine Th/*X* pairs, involving elements in the Sm–Os range. Using the predictions of the HEW *r*-process model, as given by Hayek et al. (2009), we obtained $\tau = 13.3 \pm 6.2$ Gyr from 12 Th/*X* pairs.

Based on our high-resolution spectra, covering ~4.3 years, we propose that HE 2327−5642 is a radial-velocity variable with a highly elliptical orbit of the system. Determination of the orbital period would provide the unique opportunity to determine a lower limit to the mass of the secondary in this system. Scenarios for the site of the *r*-process include a high-entropy wind from a type-II supernova (e.g., Woosley et al. 1994; Takahashi et al. 1994), ejecta from neutron star mergers (e.g. Freiburghaus et al. 1999), or the neutrino-driven wind of a newly formed neutron star in an accretion-induced collapse (AIC) event (e.g. Woosley & Baron 1992; Qian & Wasserburg 2003). According to these scenarios, it is expected that the secondary is a neutron-star. With a lower limit to the mass of the secondary, it might be possible to constrain a scenario, because in the AIC case the neutron star is expected to have a mass just slightly above the Chandrasekhar mass, while core-collapse supernovae or neutron star mergers would result in remnants of significantly higher mass.

Acknowledgements. The authors thank Thomas Gehren for the NLTE calculations for Al I and Tatyana Ryabchikova for help with collecting the atomic data. L.M. and A.V. are supported by the Russian Foundation for Basic Research (grant 08-02-92203-GFEN-a), the Russian Federal Agency on Science and Innovation (No. 02.740.11.0247), and the Swiss National Science Foundation (SCOPES project No. IZ73Z0-128180/1). N.C. is supported by the Knut and Alice Wallenberg Foundation, and by Deutsche Forschungsgemeinschaft through grants Ch 214/3 and Re 353/44. P.S.B. is a Royal Swedish Academy of Sciences Research Fellow supported by a grant from the Knut and Alice Wallenberg Foundation. P.S.B. also acknowledges additional support from the Swedish Research Council. T.C.B. acknowledges partial funding of this work from grants PHY 02-16783 and PHY 08- 22648: Physics Frontier Center/Joint Institute for Nuclear Astrophysics (JINA), awarded by the U.S. National Science Foundation. We made use of model atmosphere from the MARCS library, and the NIST and VALD databases.

References

Anders, E., & Grevesse, N. 1989, Geoch. & Cosmochim Acta, 53, 197
Andrievsky, S. M., Spite, M., Korotin, S. A., et al. 2007, A&A, 464, 1081
Andrievsky, S. M., Spite, M., Korotin, S. A., et al. 2008, A&A, 481, 481
Anstee, S. D., & O'Mara, B. J. 1995, MNRAS, 276, 859
Aoki, W., Honda, S., Beers, T. C., et al. 2005, ApJ, 632, 611
Arlandini, C., Käppeler, F., Wisshak, K., et al. 1999, ApJ, 525, 886
Asplund, M., Grevesse, N., Sauval, A. J., & Scott, P. 2009, ARAA, 47, 481
Bard, A., Kock, A., & Kock, M. 1991, A&A, 248, 315
Barklem, P. S., & Aspelund-Johansson, J. 2005, A&A, 435, 373
Barklem, P. S., & O'Mara, B. J. 1997, MNRAS, 290, 102
Barklem, P. S., & O'Mara, B. J. 1998, MNRAS, 300, 863
Barklem, P. S., O'Mara, B. J., & Ross, J. E. 1998, MNRAS, 296, 1057
Barklem, P. S., Piskunov, N., & O'Mara, B. J. 2000, A&A, 355, L5
Barklem, P. S., Christlieb, N., Beers, T. C., et al. 2005, A&A, 439, 129 (Paper II)
Baumüller, D., & Gehren, T. 1996, A&A, 307, 961
Beers, T. C., & Christlieb, N. 2005, ARA&A, 43, 531
Beers, T. C., Flynn, C., Rossi, S., et al. 2007, ApJS, 168, 128
Belyakova, E. V., & Mashonkina, L. I. 1997, Astron. Rep., 41, 530
Bergemann, M., & Gehren, T. 2007, A&A, 473, 291
Bergemann, M., & Gehren, T. 2008, A&A, 492, 823
Biémont, E., Dutrieux, J.-F., Martin, I., & Quinet, P. 1998, J. Phys., B31, 3321
Biémont, E., & Godefroid, M. 1980, A&A, 84, 361
Bizzarri, A., Huber, M. C. E., Noels, A., et al. 1993, A&A, 273, 707
Blackwell, D. E., Booth, A. J., Petford, A. D., & Laming, J. M. 1989, MNRAS, 236, 235
Booth, A. J., Blackwell, D. E., Petford, A. D., & Shallis, M. J. 1984, MNRAS, 208, 147
Bord, D. J., & Cowley, C. R. 2002, Sol. Phys., 211, 3
Borghs, G., De Bisschop, P., van Hove, M., & Silverans, R. E. 1983, Hyperfine Interactions, 15, 177
Butler, K., & Giddings, J. 1985, Newsletter on the analysis of astronomical spectra No. 9, University of London
Cardon, B. L., Smith, P. L., Scalo, J. M., & Testerman, L. 1982, ApJ, 260, 395
Cayrel, R., Hill, V., Beers, T. C., et al. 2001, Nature, 409, 691
Cayrel, R., Depagne, E., Spite, M., et al. 2004, A&A, 416, 1117
Cayrel, R., Steffen, M., Bonifacio, P., et al. 2009, Proceedings of the 10th Symposium on Nuclei in the Cosmos (NIC X), July 27−August 1, 2008 Mackinac Island, Michigan, USA
Christlieb, N., Beers, T. C., Barklem, P. S., et al. 2004, A&A, 428, 1043 (Paper I)
Christlieb, N., Schörck, T., Frebel, A., et al. 2008, A&A, 484, 721

Cowan, J. J., Sneden, C., Burles, S., et al. 2002, ApJ, 572, 861
Cowan, J. J., Sneden, C., Beers, T., et al. 2005, ApJ, 627, 238
Den Hartog, E. A., Lawler, J. E., Sneden, C., & Cowan, J. J. 2003, ApJS, 148, 543
Den Hartog, E. A., Lawler, J. E., Sneden, C., & Cowan, J. J. 2006, ApJS, 167, 292
Farouqi, K., Kratz, K.-L., Cowan, J. J., et al. 2008, AIP Conf. Proc., 990, 309
Farouqi, K., Kratz, K.-L., Mashonkina, L. I., et al. 2009, ApJ, 694, L49
François, P., Depagne, E., Hill, V., et al. 2007, A&A, 476, 935
Frebel, A., Christlieb, N., Norris, J. E., et al. 2007, ApJ, 660, L117
Freiburghaus, C., Rosswog, S., & Thielemann, F.-K. 1999, ApJ, 525, L121
Fuhr, J. R., & Wiese, W. L. 1996, NIST Atomic Transition Probability Tables, CRC Handbook of Chemistry & Physics, 77th edn., ed. D. R. Lide (Boca Raton, FL: CRC Press, Inc.)
Fuhr, J. R., Martin, G. A., & Wiese, W. L. 1988, J. Phys. Chem. Ref. Data 17, Suppl. 4
Fuhrmann, K., Pfeiffer, M., Frank, C., et al. 1997, A&A, 323, 909
Gehren, T., Liang, Y. C., Shi, J. R., et al. 2004, A&A, 413, 1045
Ginibre, A. 1989, Physica Scripta, 39, 694
Gray, D. F. 1992, The observation and analysis of stellar photospheres (Cambridge University Press)
Gustafsson, B., Edvardsson, B., Eriksson, K., et al. 2008, A&A, 486, 951
Hannaford, P., Lowe, R. M., Grevesse, N., et al. 1982, ApJ, 261, 736
Hayek, W., Wiesendahl, U., Christlieb, N., et al. 2009, A&A, 504, 511
Heiter, U., & Eriksson, K. 2006, A&A, 452, 1039
Hill, V., Plez, B., Cayrel, R., et al. 2002, A&A, 387, 560
Holt, R. A., Scholl, T. J., & Rosner, S. D. 1999, MNRAS, 306, 107
Honda, S., Aoki, W., Kajino, T., et al. 2004, ApJ, 607, 474
Honda, S., Aoki, W., Ishimaru, Y., et al. 2006, ApJ, 643, 1180
Honda, S., Aoki, W., Ishimaru, Y., et al. 2007, ApJ, 666, 1189
Huber, M. C. E., & Sandeman, R. J. 1980, A&A, 86, 95
Iben, I. Jr. 1967, ApJ, 147, 624
Ivans, I. I., Simmerer, J., Sneden, C., et al. 2006, ApJ, 645, 613
Ivarsson, S., Litzén, U., & Wahlgren, G. 2001, Phys. Scr., 64, 455
Ivarsson, S., Andersen, J., Nordström, B., et al. 2003, A&A, 409, 1141
Johnson, J. A. 2002, ApJS, 139, 219
Jonsell, K., Barklem, P. S., Gustafsson, B., et al. 2006, A&A, 451, 651
Kamp, I., Korotin, S., Mashonkina, L., et al. 2003, in Modelling of Stellar Atmospheres, Uppsala, 17−21 June 2002, ed. N. Piskunov, W. W. Weiss, & D. F. Gray, Proc. IAU Symp., 210, 323
Kling, R., & Griesmann, U. 2000, ApJ, 531, 1173
Kupka, F., Piskunov, N., Ryabchikova, T. A., et al. 1999, A&AS, 138, 119
Kurucz, R. L. 1993, SYNTHE Spectrum Synthesis Programs and Line Data, Kurucz CD-ROM No. 18 (Cambridge, Mass.: Smithsonian Astrophysical Observatory), 18
Kurucz, R. L. 1994, Opacities for Stellar Atmospheres, CD-ROM No. 2−8 (Cambridge, Mass.: Smithsonian Astrophysical Observatory), 2
Kurucz, R. L. 2004, Mem.S.A.It., 75, 1
Kurucz, R. L., & Bell, B. 1995, Atomic Line Data. Kurucz CD-ROM No. 23 (Cambridge, Mass: Smithsonian Astrophysical Observatory), 23
Kurucz, R. L., Furenlid, I., Brault, J., & Testerman, L. 1984, Solar Flux Atlas from 296 to 1300 nm, Nat. Solar Obs., Sunspot, New Mexico
Lai, D. K., Bolte, M., Johnson, J. A., et al. 2008, ApJ, 681, 1524
Lawler, J. E., & Dakin, J. T. 1989, J. Opt. Soc. Am. B, 6, 1457
Lawler, J. E., Bonvallet, G., & Sneden, C. 2001a, ApJ, 556, 452
Lawler, J. E., Wickliffe, M. E., Den Hartog, E. A., & Sneden, C. 2001b, ApJ, 563, 1075
Lawler, J. E., Wickliffe, M. E., Cowley, C. R., & Sneden, C. 2001c, ApJS, 137, 341
Lawler, J. E., Wyart, J.-F., & Blaise, J. 2001d, ApJS, 137, 351
Lawler, J. E., Sneden, C., & Cowan, J. J. 2004, ApJ, 604, 850
Lawler, J. E., Den Hartog, E. A., Sneden, C., & Cowan, J. J. 2006, ApJS, 162, 227
Lawler, J. E., Den Hartog, E. A., Labby, Z. E., et al. 2007, ApJS, 169, 120
Lawler, J. E., Sneden, C., Cowan, J. J., et al. 2008, ApJS, 178, 71
Lawler, J. E., Sneden, C., Cowan, J. J., et al. 2009, ApJS, 182, 51
Lefébvre, P.-H., Garnir, H.-P., & Biémont, E. 2003, A&A, 404, 1153
Lind, K., Asplund, M., & Barklem, P. S. 2009, A&A, 503, 541
Ljung, G., Nilsson, H., Asplund, M., & Johansson, S. 2006, A&A, 456, 1181
Lodders, K. 2003, ApJ, 591, 1220
Lodders, K., Palme, H., & Gail, H.-P. 2009, in Landolt-Börnstein, New Series (Berlin: Springer Verlag), [0901.1149]
Malcheva, G., Blagoev, K., Mayo, R., et al. 2006, MNRAS, 367,754
Martin, G. A., Fuhr, J. R., & Wiese, W. L. 1988, J. Phys. Chem. Ref. Data, 17, Suppl., 3
Mårtensson-Pendrill, A.-M., Gough, D. S., & Hannaford, P. 1994, Phys. Rev. A, 49, 3351
Mashonkina, L. I., & Gehren, T. 2000, A&A, 364, 249
Mashonkina, L. I., Sakhibullin, N. A., & Shimansky, V. V. 1993, Astron. Rep., 37, 192
Mashonkina, L. I., Gehren, T., & Bikmaev, I. F. 1999, A&A, 343, 519
Mashonkina, L. I., Korn, A. J., & Przybilla, N. 2007a, A&A, 461, 261
Mashonkina, L., Vinogradova, A., Ptitsyn, D., et al. 2007b, Astron. Rep., 84, 997
Mashonkina, L., Zhao, G., Gehren, T., et al. 2008, A&A, 478, 529
Mashonkina, L., Ryabchikova, T. A., Ryabtsev, A. N., & Kildiyarova, R. 2009, A&A, 495, 297
Mashonkina, L. I., Gehren, T., Shi, J., et al. 2010, Chemical Abundances in the Universe: Connecting First Stars to Planets, Proc. IAU Symp., 265, 197 [0910.3997]
McWilliam, A. 1998, AJ, 115, 1640
McWilliam, A., Preston, G. W., Sneden, C., et al. 1995, AJ, 109, 2757
Meléndez, J., & Barbuy, B. 2009, A&A, 497, 611
Nilsson, H., Zhang, Z. G., Lundberg, H., et al. 2002, A&A, 382, 368
Nitz, D. E., Kunau, A. E., Wilson, K. L., & Lentz, L. R. 1999, ApJS, 122, 557
Nörtershäuser, W., Blaum, K., Icker, K., et al. 1998, Eur. Phys. J., D2, 33
O'Brian, T. R., & Lawler, J. E. 1991, Phys. Rev. A, 44, 7134
O'Brian, T. R., Wickliffe, M. E., Lawler, J. E., et al. 1991, J. Opt. Soc. Am. B, 8, 1185
Pickering, J. C. 1996, ApJS, 107, 811
Pickering, J. C., Thorne, A. P., & Perez, R. 2001, ApJS, 132, 403
Plez, B., Hill, V., Cayrel, R., et al. 2004, A&A, 428, L9
Ralchenko, Yu., Kramida, A. E., Reader, J., & NIST ASD Team. 2008, NIST Atomic Spectra Database (version 3.1.5), available: http://physics.nist.gov/asd3, NIST, Gaithersburg, MD.
Qian, Y.-Z., & Wasserburg, G. J. 2003, ApJ, 588, 1099
Qian, Y.-Z., & Wasserburg, G. J. 2008, ApJ, 687, 272
Reader, J., Corliss, C. H., Wiese, W. L., & Martin, G. A. 1980, Wavelengths and Transition Probabilities for Atoms and Atomic Ions. Part II. NSRDS - NBS 68, Washington, D.C.
Reetz, J. K. 1991, Diploma Thesis, Universität München
Roederer, I. U., Lawler, J. E., Sneden, C., et al. 2008, ApJ, 675, 723
Roederer, I. U., Kratz, K.-L., Frebel, A., et al. 2009, ApJ, 698, 1963
Sakhibullin, N. A. 1983, Trudi Kazan gor.obs., 48, 9
Sansonetti, C. J., Richou, B., Engleman, R. Jr., & Radziemski, L. J. 1995, Phys. Rev. A, 52, 2682
Schlegel, D. J., Finkbeiner, D. P., & Davis, M. 1998, ApJ, 500, 525
Shi, J. R., Gehren, T., Mashonkina, L., & Zhao, G. 2009, A&A, 503, 533
Smith, G. 1981, A&A, 103, 351
Smith, G., & O'Neil, J. A. 1975, A&A, 38, 1
Smith, G., & Raggett, D. St. J. 1981, J. Phys., B14, 4015
Sneden, C. 1973, ApJ, 184, 839
Sneden, C., Preston, G. W., McWilliam, A., & Searle, L. 1994, ApJ, 431, L27
Sneden, C., McWilliam, A., Preston, G. W., et al. 1996, ApJ, 467, 819
Sneden, C., Cowan, J. J., Lawler, J. E., et al. 2003, ApJ, 591, 936
Sneden, C., Lawler, J. E., Cowan, J. J., et al. 2009, ApJS, 182, 80
Spergel, D. N., Verde, L., & Peiris, H. V. 2003, ApJS, 148, 175
Spite, M., & Spite, F. 1978, A&A, 67, 23
Steenbock, W., & Holweger, H. 1984, A&A, 130, 319
Takahashi, K., Witti, J., & Janka, H.-T. 1994, A&A, 286, 857
Takeda, Y., Hashimoto, O., Taguchi, H., et al. 2005, PASJ, 57,751
Theodosiou, C. E. 1989, Phys. Rev., A39, 4880
Travaglio, C., Galli, D., Gallino, R., et al. 1999, ApJ, 521, 691
Travaglio, C., Gallino, R., Arnone, E., et al. 2004, ApJ, 601, 864
Truran, J. W. 1981, A&A, 97, 391
Truran, J. W., Cowan, J. J., Pilachowski, C. A., & Sneden, C. 2002, PASP, 114, 1293
van Kleef, Th. A. M., & Metsch, B. C. 1978, Phys. 95C, 251
Velichko, A., Mashonkina, L., & Nilsson, H. 2010, Astron. Let. (in press)
Vidal, C. R., Cooper, J., & Smith, E. W. 1970, JQSRT, 10, 1011
Vidal, C. R., Cooper, J., & Smith, E. W. 1973, ApJS, 25, 37
Wickliffe, M. E., & Lawler, J. E. 1997a, ApJS, 110, 163
Wickliffe, M. E., & Lawler, J. E. 1997b, J. Opt. Soc. Am., B 14, 737
Wickliffe, M. E., Lawler, J. E., & Nave, G. 2000, JQSRT 66, 363
Wiese, W. L., & Fuhr, J. R. 1975, J. Phys. Chem. Ref. Data, 4, 263
Woosley, S. E., & Baron, E. 1992, ApJ, 391, 228
Woosley, S. E., Wilson, J. R., Mathews, G. J., et al. 1994, ApJ, 433, 229
Xu, H. L., Sun, Z. W., Dai, Z. W., et al. 2006, A&A, 452, 357
Zhang, H. W., Gehren, T., & Zhao, G. 2008, A&A, 481, 489
Zhao, G., Butler, K., & Gehren, T. 1998, A&A, 333, 219

Pages 16 to 22 are available in the electronic edition of the journal at http://www.aanda.org

Table 8. Line data and abundances from an analysis of HE 2327−5642. Γ_6 corresponds to 10 000 K. Column 6 gives references to the adopted gf−values. Column 13 gives references to the sources of the used IS and HFS data and adopted Γ_6−values.

Z	Atom/ mol	λ (Å)	E_{exc} (eV)	$\log gf$	Ref	$\log \varepsilon$ Solar	$\log \varepsilon$ LTE	$\log \varepsilon$ NLTE	[X/Fe]	W_λ (mÅ)	$\log \Gamma_6/N_H$ (rad/s·cm^3)	Note, Ref.
1	2	3	4	5	6	7	8	9	10	11	12	13
3	Li 1	6707.80	0.00	0.167	NIST8	1.10	0.99		2.67	Syn	−7.574	IS:SRE95 Γ_6:ABO
6	CH	4310.0–4312.5			BCB05	8.39	5.74		0.13	Syn		
6	CH	4313.4–4313.8			BCB05	8.39	5.74		0.13	Syn		
6	CH	4362.4–4364.6			BCB05	8.39	5.76		0.15	Syn		
6	CH	4366.0–4367.0			BCB05	8.39	5.73		0.12	Syn		
7	NH	3358–3361			K94	7.86	4.78		−0.30	Syn		
11	Na 1	5889.96	0.00	0.110	NIST8	6.30	3.28	2.89	−0.63	Syn	−7.712	Γ_6:GLS04
11	Na 1	5895.93	0.00	−0.190	NIST8	6.30	3.24	2.96	−0.56	Syn	−7.712	the same
12	Mg 1	4571.10	0.00	−5.620	NIST8	7.54	4.86	4.98	0.22	Syn	−7.856	Γ_6:GLS04
12	Mg 1	4702.99	4.33	−0.440	NIST8	7.54	4.79	4.90	0.14	Syn	−6.956	the same
12	Mg 1	5528.41	4.33	−0.498	NIST8	7.54	4.84	4.96	0.20	Syn	−7.152	the same
13	Al 1	3961.52	0.01	−0.340	NIST8	6.47	2.50	3.02	−0.67	Syn	−7.552	Γ_6:GLS04
14	Si 1	3905.53	1.91	−1.041	BL91	7.52	4.85		0.11	Syn	−7.440	Γ_6:ABO
20	Ca 1	4425.44	1.88	−0.358	SON75	6.33	3.52	3.76	0.20	23.7	−7.432	Γ_6:MKP07
20	Ca 1	5349.46	2.71	−0.310	SR81	6.33	3.52	3.78	0.21	4.6	−7.652	Γ_6:S81
20	Ca 1	5588.75	2.53	0.358	SR81	6.33	3.57	3.86	0.26	22.8	−7.628	Γ_6:S81
20	Ca 1	5857.45	2.93	0.240	SR81	6.33	3.67	3.86	0.36	11.2	−7.316	Γ_6:S81
20	Ca 1	6122.22	1.89	−0.315	SON75	6.33	3.68	3.90	0.36	29.5	−7.189	Γ_6:ABO
20	Ca 1	6162.17	1.90	−0.089	SON75	6.33	3.63	3.84	0.32	38.6	−7.189	Γ_6:ABO
20	Ca 1	6169.56	2.53	−0.478	SR81	6.33	3.52	3.81	0.21	4.7	−7.264	Γ_6:S81
20	Ca 1	6439.08	2.53	0.390	SR81	6.33	3.63	3.80	0.31	27.4	−7.704	Γ_6:S81
20	Ca 2	8498.02	1.69	−1.416	Th89	6.33	–	3.82	0.27	Syn	−7.676	IS:NBI98 Γ_6:ABO
21	Sc 2	4246.82	0.32	0.240	LD89	3.10	0.08		−0.24	Syn		HFS:MPS95
21	Sc 2	4400.39	0.60	−0.540	LD89	3.10	0.08		−0.24	Syn		the same
21	Sc 2	4415.56	0.60	−0.670	LD89	3.10	0.13		−0.19	Syn		the same
21	Sc 2	5031.02	1.36	−0.400	LD89	3.10	0.09		−0.23	Syn		the same
22	Ti 1	3998.64	0.05	−0.056	WF75	4.90	2.14		0.02	37.3	−7.654	Γ_6:ABO
22	Ti 1	4533.25	0.85	0.476	WF75	4.90	2.06		−0.06	19.7	−7.593	the same
22	Ti 1	4534.78	0.84	0.280	WF75	4.90	2.01		−0.11	12.5	−7.596	the same
22	Ti 1	4981.73	0.85	0.504	WF75	4.90	2.15		0.03	25.6	−7.626	the same
22	Ti 1	4991.06	0.84	0.380	WF75	4.90	2.15		0.03	21.0	−7.629	the same
22	Ti 1	5022.87	0.83	−0.434	WF75	4.90	2.14		0.02	3.9	−7.633	the same
22	Ti 1	5024.85	0.82	−0.602	WF75	4.90	2.32		0.20	4.1	−7.635	the same
22	Ti 1	5039.96	0.02	−1.130	WF75	4.90	2.09		−0.03	5.7	−7.720	the same
22	Ti 1	5064.66	0.05	−0.991	WF75	4.90	2.18		0.06	8.8	−7.719	the same
22	Ti 1	5210.39	0.05	−0.884	WF75	4.90	2.21		0.09	11.8	−7.724	the same
22	Ti 2	3913.47	1.12	−0.420	PTP01	4.90	2.29		0.17	87.4		
22	Ti 2	4028.34	1.89	−0.960	PTP01	4.90	2.25		0.13	21.8		
22	Ti 2	4053.83	1.89	−1.130	PTP01	4.90	2.11		−0.01	11.9		
22	Ti 2	4290.22	1.16	−0.850	PTP01	4.90	2.16		0.04	66.5		
22	Ti 2	4300.05	1.18	−0.440	PTP01	4.90	2.41		0.29	93.3		
22	Ti 2	4394.05	1.22	−1.780	PTP01	4.90	2.24		0.12	20.5		
22	Ti 2	4395.03	1.08	−0.540	PTP01	4.90	2.22		0.10	88.0		
22	Ti 2	4395.85	1.24	−1.930	PTP01	4.90	2.29		0.17	16.2		
22	Ti 2	4399.77	1.24	−1.190	PTP01	4.90	2.29		0.17	51.4		
22	Ti 2	4417.72	1.16	−1.190	PTP01	4.90	2.23		0.11	53.0		
22	Ti 2	4418.33	1.24	−1.970	PTP01	4.90	2.23		0.11	13.3		
22	Ti 2	4443.79	1.08	−0.720	PTP01	4.90	2.22		0.10	79.9		
22	Ti 2	4444.56	1.12	−2.240	PTP01	4.90	2.29		0.17	11.7		
22	Ti 2	4450.48	1.08	−1.520	PTP01	4.90	2.24		0.12	40.2		
22	Ti 2	4464.45	1.16	−1.810	PTP01	4.90	2.33		0.21	26.0		
22	Ti 2	4468.51	1.13	−0.600	BHN93	4.90	2.20		0.08	81.8		

Table 8. continued.

Z	Atom/ mol	λ (Å)	E_{exc} (eV)	$\log gf$	Ref	$\log\varepsilon$ Solar	$\log\varepsilon$ LTE	$\log\varepsilon$ NLTE	[X/Fe]	W_λ (mÅ)	$\log\Gamma_6/N_H$ (rad/s·cm^3)	Note, Ref.
1	2	3	4	5	6	7	8	9	10	11	12	13
22	Ti 2	4470.86	1.16	−2.020	PTP01	4.90	2.07		−0.05	10.6		
22	Ti 2	4501.27	1.12	−0.770	PTP01	4.90	2.23		0.11	77.5		
22	Ti 2	4533.97	1.24	−0.530	PTP01	4.90	2.10		−0.02	76.0		
22	Ti 2	4563.76	1.22	−0.690	PTP01	4.90	2.05		−0.07	67.7		
22	Ti 2	4571.97	1.57	−0.320	PTP01	4.90	2.08		−0.04	67.7		
22	Ti 2	5185.91	1.89	−1.490	PTP01	4.90	2.14		0.02	7.3		
22	Ti 2	5188.70	1.58	−1.050	PTP01	4.90	2.20		0.08	36.4		
22	Ti 2	5226.55	1.57	−1.260	PTP01	4.90	2.21		0.09	26.9		
22	Ti 2	5336.79	1.58	−1.590	PTP01	4.90	2.20		0.08	14.3		
22	Ti 2	5381.01	1.57	−1.920	PTP01	4.90	2.15		0.03	6.6		
23	V 2	3530.76	1.07	−0.600	FW96	4.00	0.84		−0.38	Syn		
23	V 2	3545.19	1.10	−0.390	FW96	4.00	0.84		−0.38	Syn		
23	V 2	3592.03	1.10	−0.370	FW96	4.00	0.88		−0.34	Syn		
23	V 2	4005.71	1.82	−0.460	FW96	4.00	1.01		−0.21	Syn		
24	Cr 1	4254.33	0.00	−0.114	MFW88	5.64	2.22		−0.64	80.4	−7.675	Γ_6:ABO
24	Cr 1	4274.80	0.00	−0.230	MFW88	5.64	2.16		−0.70	73.9	−7.675	the same
24	Cr 1	5206.04	0.94	0.019	MFW88	5.64	2.31		−0.55	45.1	−7.597	the same
24	Cr 1	5345.81	1.00	−0.980	MFW88	5.64	2.43		−0.43	8.7	−7.620	the same
24	Cr 1	5348.33	1.00	−1.290	FW96	5.64	2.34		−0.52	3.6	−7.620	the same
24	Cr 1	5409.80	1.03	−0.720	MFW88	5.64	2.44		−0.42	14.1	−7.620	the same
25	Mn 1	4030.75	0.00	−0.470	BBP84	5.37	1.53		−1.06	Syn	−7.552	HFS:LGB03 Γ_6:ABO
25	Mn 1	4033.06	0.00	−0.620	BBP84	5.37	1.53		−1.06	Syn	−7.552	the same
25	Mn 1	4034.48	0.00	−0.810	BBP84	5.37	1.53		−1.06	Syn	−7.552	the same
25	Mn 1	4041.35	2.11	0.280	BBP84	5.37	1.89		−0.70	Syn	−7.701	Γ_6:ABO
25	Mn 2	3460.31	1.81	−0.640	KG00	5.37	1.91		−0.68	Syn		HFS:HSR99
25	Mn 2	3482.90	1.83	−0.840	KG00	5.37	1.94		−0.65	Syn		HFS:HSR99
25	Mn 2	3488.67	1.85	−0.950	KG00	5.37	2.10		−0.49	Syn		HFS:HSR99
26	Fe 1	3917.18	0.99	−2.155	OWL91	7.45	4.61	4.69	0.02	65.3	−7.695	Γ_6:ABO
26	Fe 1	3949.95	2.18	−1.251	OWL91	7.45	4.39	4.47	−0.19	36.8	−7.820	the same
26	Fe 1	4005.24	1.56	−0.580	OWL91	7.45	4.66	4.72	0.07	96.1	−7.620	the same
26	Fe 1	4132.06	1.61	−0.675	OWL91	7.45	4.61	4.68	0.02	94.3	−7.620	the same
26	Fe 1	4132.90	2.85	−1.006	OWL91	7.45	4.53	4.61	−0.06	19.4	−7.659	the same
26	Fe 1	4143.87	1.56	−0.511	OWL91	7.45	4.53	4.59	−0.06	98.0	−7.636	the same
26	Fe 1	4147.67	1.49	−2.074	OWL91	7.45	4.68	4.76	0.10	40.3	−7.648	the same
26	Fe 1	4202.03	1.49	−0.708	FMW88	7.45	4.64	4.67	0.05	98.4	−7.648	the same
26	Fe 1	4216.18	0.00	−3.356	FMW88	7.45	4.66	4.75	0.08	69.5	−7.797	the same
26	Fe 1	4250.79	1.56	−0.714	OWL91	7.45	4.69	4.73	0.10	95.9	−7.648	the same
26	Fe 1	4260.47	2.40	0.080	OWL91	7.45	4.45	4.51	−0.14	86.1	−7.274	the same
26	Fe 1	4415.12	1.61	−0.615	FMW88	7.45	4.56	4.61	−0.02	99.0	−7.652	the same
26	Fe 1	4427.31	0.05	−2.924	OWL91	7.45	4.77	4.86	0.18	87.6	−7.813	the same
26	Fe 1	4602.94	1.49	−2.209	OWL91	7.45	4.55	4.63	−0.04	36.3	−7.790	the same
26	Fe 1	4647.43	2.95	−1.351	OWL91	7.45	4.49	4.57	−0.10	7.9	−7.685	the same
26	Fe 1	4966.09	3.33	−0.871	OWL91	7.45	4.59	4.69	0.00	11.4	−7.218	the same
26	Fe 1	4994.13	0.92	−2.970	OWL91	7.45	4.63	4.72	0.04	31.4	−7.744	the same
26	Fe 1	5001.86	3.88	0.010	FMW88	7.45	4.57	4.67	−0.02	13.9	−7.273	the same
26	Fe 1	5014.94	3.94	−0.303	OWL91	7.45	4.59	4.68	0.00	8.7	−7.268	Γ_6:ABO
26	Fe 1	5051.63	0.92	−2.765	OWL91	7.45	4.71	4.80	0.12	48.0	−7.746	the same
26	Fe 1	5068.77	2.94	−1.042	OWL91	7.45	4.56	4.65	−0.03	14.1	−7.265	the same
26	Fe 1	5150.84	0.99	−3.040	OWL91	7.45	4.67	4.75	0.08	23.0	−7.742	the same
26	Fe 1	5166.28	0.00	−4.200	OWL91	7.45	4.69	4.78	0.10	33.5	−7.826	the same
26	Fe 1	5171.60	1.49	−1.720	OWL91	7.45	4.81	4.89	0.22	63.8	−7.687	the same
26	Fe 1	5192.34	3.00	−0.421	OWL91	7.45	4.53	4.61	−0.06	34.7	−7.266	the same
26	Fe 1	5194.94	1.56	−2.020	OWL91	7.45	4.67	4.75	0.08	41.0	−7.680	the same
26	Fe 1	5216.27	1.61	−2.080	OWL91	7.45	4.69	4.77	0.10	37.3	−7.674	the same
26	Fe 1	5281.79	3.04	−0.830	OWL91	7.45	4.65	4.73	0.06	18.4	−7.266	the same
26	Fe 1	5283.62	3.24	−0.520	OWL91	7.45	4.48	4.57	−0.11	21.8	−7.221	the same
26	Fe 1	5324.18	3.21	−0.100	BKK91	7.45	4.35	4.44	−0.24	35.1	−7.235	the same
26	Fe 1	5339.93	3.27	−0.720	OWL91	7.45	4.48	4.57	−0.11	14.5	−7.221	the same
26	Fe 1	5364.87	4.45	0.228	OWL91	7.45	4.47	4.58	−0.12	5.3	−7.136	the same
26	Fe 1	5367.47	4.41	0.440	OWL91	7.45	4.56	4.67	−0.03	8.9	−7.153	the same

Table 8. continued.

Z	Atom/ mol	λ (Å)	E_{exc} (eV)	$\log gf$	Ref	$\log \varepsilon$			[X/Fe]	W_λ (mÅ)	$\log \Gamma_6/N_H$ (rad/s·cm^3)	Note, Ref.
						Solar	LTE	NLTE				
1	2	3	4	5	6	7	8	9	10	11	12	13
26	Fe 1	5369.96	4.37	0.536	OWL91	7.45	4.58	4.69	−0.01	12.3	−7.179	the same
26	Fe 1	5383.37	4.31	0.645	OWL91	7.45	4.57	4.69	−0.02	16.8	−7.219	the same
26	Fe 1	5393.17	3.24	−0.720	BKK91	7.45	4.56	4.64	−0.03	15.2	−7.235	the same
26	Fe 1	5410.91	4.47	0.398	OWL91	7.45	4.62	4.73	0.03	7.5	−7.132	the same
26	Fe 1	5415.20	4.39	0.642	OWL91	7.45	4.52	4.63	−0.07	13.4	−7.182	the same
26	Fe 1	5434.52	1.01	−2.130	OWL91	7.45	4.77	4.85	0.18	80.4	−7.749	the same
26	Fe 1	5445.04	4.39	−0.020	FMW88	7.45	4.58	4.69	−0.01	5.7	−7.189	the same
26	Fe 1	5506.78	0.99	−2.797	OWL91	7.45	4.70	4.79	0.11	44.6	−7.753	the same
26	Fe 1	5586.76	3.37	−0.100	BKK91	7.45	4.42	4.51	−0.17	29.4	−7.221	the same
26	Fe 1	5615.64	3.33	0.050	BKK91	7.45	4.41	4.50	−0.18	37.2	−7.234	the same
26	Fe 1	6136.62	2.45	−1.410	OWL91	7.45	4.50	4.58	−0.09	25.2	−7.609	the same
26	Fe 1	6137.69	2.59	−1.350	OWL91	7.45	4.46	4.54	−0.13	19.1	−7.589	the same
26	Fe 1	6191.56	2.43	−1.417	OWL91	7.45	4.55	4.63	−0.04	24.4	−7.615	the same
26	Fe 1	6393.60	2.43	−1.570	OWL91	7.45	4.44	4.52	−0.14	20.0	−7.622	the same
26	Fe 1	6400.00	3.60	−0.290	BKK91	7.45	4.46	4.55	−0.13	14.0	−7.232	the same
26	Fe 1	6430.85	2.18	−1.950	OWL91	7.45	4.63	4.71	0.04	18.0	−7.704	the same
26	Fe 2	4508.29	2.86	−2.440	MB09	7.45	4.64	4.64	−0.03	22.6	−7.870	the same
26	Fe 2	4515.34	2.84	−2.600	MB09	7.45	4.81	4.81	0.14	21.2	−7.880	the same
26	Fe 2	4520.22	2.81	−2.650	MB09	7.45	4.61	4.61	−0.06	17.6	−7.880	the same
26	Fe 2	4923.93	2.89	−1.260	MB09	7.45	4.59	4.58	−0.07	68.5	−7.890	the same
26	Fe 2	5018.44	2.89	−1.100	MB09	7.45	4.64	4.63	−0.02	77.9	−7.890	the same
26	Fe 2	5197.58	3.23	−2.220	MB09	7.45	4.69	4.69	0.03	14.6	−7.880	the same
26	Fe 2	5234.62	3.22	−2.180	MB09	7.45	4.70	4.70	0.03	17.6	−7.880	the same
26	Fe 2	5284.11	2.89	−3.110	MB09	7.45	4.73	4.73	0.06	5.6	−7.890	the same
27	Co 1	3412.33	0.51	0.030	CSS82	4.92	1.87		−0.27	Syn	−7.666	HFS:P96 Γ_6:ABO
27	Co 1	3417.16	0.58	−0.470	CSS82	4.92	1.97		−0.17	Syn	−7.657	Γ_6:ABO
27	Co 1	3489.40	0.92	0.150	CSS82	4.92	1.86		−0.28	Syn	−7.610	HFS:P96 Γ_6:ABO
27	Co 1	3894.07	1.05	0.090	NKW99	4.92	1.98		−0.16	Syn	−7.648	HFS:P96 Γ_6:ABO
27	Co 1	4118.77	1.05	−0.470	NKW99	4.92	2.05		−0.09	Syn	−7.710	Γ_6:ABO
27	Co 1	4121.31	0.92	−0.300	NKW99	4.92	2.05		−0.09	Syn	−7.724	HFS:P96 Γ_6:ABO
28	Ni 1	3413.47	0.16	−1.480	HS80	6.23	3.18		−0.27	Syn	−7.690	Γ_6:ABO
28	Ni 1	3413.93	0.11	−1.720	FMW88	6.23	3.26		−0.19	Syn	−7.785	the same
28	Ni 1	3519.76	0.28	−1.420	BBP89	6.23	3.08		−0.37	Syn	−7.689	the same
28	Ni 1	3783.52	0.42	−1.310	HS80	6.23	3.00		−0.45	Syn	−7.780	the same
28	Ni 1	3807.14	0.42	−1.220	BBP89	6.23	3.00		−0.45	Syn	−7.694	the same
28	Ni 1	3858.29	0.42	−0.950	BBP89	6.23	2.98		−0.47	Syn	−7.700	the same
28	Ni 1	5035.37	3.63	0.290	WL97a	6.23	3.09		−0.36	Syn	−7.231	Γ_6:ABO
28	Ni 1	5476.90	1.83	−0.890	FMW88	6.23	3.20		−0.25	Syn		
30	Zn 1	4722.16	4.01	−0.390	BG80	4.62	1.82		−0.02	Syn		
30	Zn 1	4810.54	4.06	−0.170	BG80	4.62	1.84		0.00	Syn		
38	Sr 2	4077.72	0.00	0.150	RCW80	2.92	−0.01	−0.16	−0.30	Syn	−7.792	HFS:BBH83 Γ_6:MZG08
38	Sr 2	4215.54	0.00	−0.170	RCW80	2.92	−0.01	−0.16	−0.30	Syn	−7.792	the same
39	Y 2	3549.01	0.13	−0.280	HLG82	2.21	−0.74		−0.17	Syn		
39	Y 2	3600.74	0.18	0.280	HLG82	2.21	−0.67		−0.10	Syn		
39	Y 2	3611.04	0.13	0.010	HLG82	2.21	−0.73		−0.16	Syn		
39	Y 2	3774.33	0.13	0.210	HLG82	2.21	−0.67		−0.10	Syn		
39	Y 2	3788.69	0.10	−0.070	HLG82	2.21	−0.66		−0.09	Syn		
39	Y 2	3950.35	0.10	−0.490	HLG82	2.21	−0.56		0.01	Syn		
39	Y 2	4883.68	1.08	0.070	HLG82	2.21	−0.66		−0.09	Syn		
39	Y 2	5087.43	1.08	−0.170	HLG82	2.21	−0.75		−0.18	Syn		
39	Y 2	5205.73	1.03	−0.340	HLG82	2.21	−0.75		−0.18	Syn		
40	Zr 2	3404.83	0.36	−0.490	LNA06	2.58	−0.01	0.07	0.26	Syn		
40	Zr 2	3430.53	0.47	−0.160	LNA06	2.58	−0.03	0.08	0.28	Syn		
40	Zr 2	3457.56	0.56	−0.470	MBM06	2.58	0.06	0.14	0.34	Syn		

Table 8. continued.

Z	Atom/ mol	λ (Å)	E_{exc} (eV)	$\log gf$	Ref	$\log\varepsilon$ Solar	$\log\varepsilon$ LTE	$\log\varepsilon$ NLTE	[X/Fe]	W_λ (mÅ)	$\log\Gamma_6/N_H$ (rad/s·cm^3)	Note, Ref.
1	2	3	4	5	6	7	8	9	10	11	12	13
40	Zr 2	3479.39	0.71	−0.180	LNA06	2.58	0.02	0.16	0.36	Syn		
40	Zr 2	3499.57	0.41	−1.060	LNA06	2.58	−0.02	0.02	0.22	Syn		
40	Zr 2	3505.67	0.16	−0.390	LNA06	2.58	−0.02	0.03	0.23	Syn		
40	Zr 2	3551.95	0.09	−0.360	LNA06	2.58	0.01	0.07	0.27	Syn		
40	Zr 2	3573.08	0.32	−0.910	MBM06	2.58	0.09	0.18	0.38	Syn		
40	Zr 2	3766.82	0.41	−0.830	LNA06	2.58	0.12	0.16	0.36	Syn		
40	Zr 2	3998.97	0.56	−0.520	LNA06	2.58	0.07	0.15	0.35	Syn		
40	Zr 2	4161.21	0.71	−0.590	LNA06	2.58	0.08	0.16	0.36	Syn		
40	Zr 2	4208.98	0.71	−0.510	LNA06	2.58	0.07	0.15	0.35	Syn		
42	Mo 1	3864.11	0.00	−0.010	FW96	1.92	−0.49		0.37	Syn		
46	Pd 1	3404.58	0.81	0.330	XSD06	1.66	−0.72		0.40	Syn		
56	Ba 2	4554.03	0.00	0.167	RCW80	2.17	−0.16	−0.25	0.36	Syn	−7.732	HFS:M98 Γ_6:MZG08
56	Ba 2	5853.67	0.60	−1.000	RCW80	2.17	−0.29	−0.23	0.38	Syn	−7.584	Γ_6:ABO
56	Ba 2	6141.71	0.70	−0.076	RCW80	2.17	−0.34	−0.36	0.25	Syn	−7.584	Γ_6:ABO
56	Ba 2	6496.90	0.60	−0.377	RCW80	2.17	−0.28	−0.32	0.29	Syn	−7.584	Γ_6:ABO
57	La 2	3849.01	0.00	−0.450	LBS01	1.14	−1.11		0.53	Syn		HFS:LBS01
57	La 2	3949.10	0.40	0.490	LBS01	1.14	−1.13		0.51	Syn		HFS:LBS01
57	La 2	3988.51	0.40	0.210	LBS01	1.14	−1.13		0.51	Syn		HFS:LBS01
57	La 2	3995.74	0.17	−0.060	LBS01	1.14	−1.09		0.55	Syn		HFS:LBS01
57	La 2	4077.34	0.24	−0.060	LBS01	1.14	−1.11		0.53	Syn		HFS:LBS01
57	La 2	4086.71	0.00	−0.070	LBS01	1.14	−1.06		0.58	Syn		HFS:LBS01
57	La 2	4196.55	0.32	−0.300	LBS01	1.14	−1.11		0.53	Syn		HFS:LBS01
57	La 2	4920.98	0.13	−0.580	LBS01	1.14	−1.08		0.56	Syn		HFS:LBS01
58	Ce 2	3942.15	0.00	−0.220	LSC09	1.61	−0.60		0.57	Syn		
58	Ce 2	3992.38	0.45	−0.220	LSC09	1.61	−0.57		0.60	Syn		
58	Ce 2	3993.82	0.91	0.290	LSC09	1.61	−0.59		0.58	Syn		
58	Ce 2	3999.24	0.30	0.060	LSC09	1.61	−0.67		0.50	Syn		
58	Ce 2	4073.47	0.48	0.210	LSC09	1.61	−0.69		0.48	Syn		
58	Ce 2	4075.70	0.70	0.230	LSC09	1.61	−0.68		0.49	Syn		
58	Ce 2	4083.22	0.70	0.270	LSC09	1.61	−0.58		0.59	Syn		
58	Ce 2	4127.36	0.68	0.310	LSC09	1.61	−0.70		0.47	Syn		
58	Ce 2	4137.64	0.52	0.400	LSC09	1.61	−0.55		0.62	Syn		
58	Ce 2	4222.60	0.12	−0.150	LSC09	1.61	−0.59		0.58	Syn		
58	Ce 2	4562.36	0.48	0.210	LSC09	1.61	−0.68		0.49	Syn		
58	Ce 2	4628.16	0.52	0.140	LSC09	1.61	−0.63		0.54	Syn		
59	Pr 2	4143.12	0.37	0.610	ILW01	0.76	−1.21	−1.13	0.89	Syn		HFS:G89
59	Pr 2	4179.40	0.20	0.480	ILW01	0.76	−1.09	−1.01	1.01	Syn		HFS:G89
59	Pr 2	4408.82	0.00	0.180	ILW01	0.76	−1.14	−1.07	0.95	Syn		HFS:G89
60	Nd 2	3784.25	0.38	0.150	DLS03	1.45	−0.78		0.55	Syn		
60	Nd 2	3838.98	0.00	−0.240	DLS03	1.45	−0.68		0.65	Syn		
60	Nd 2	3900.22	0.47	0.100	DLS03	1.45	−0.70		0.63	Syn		
60	Nd 2	3941.51	0.06	−0.020	DLS03	1.45	−0.64		0.69	Syn		
60	Nd 2	3990.10	0.47	0.130	DLS03	1.45	−0.68		0.65	Syn		
60	Nd 2	3991.74	0.00	−0.260	DLS03	1.45	−0.63		0.70	Syn		
60	Nd 2	4012.70	0.00	−0.600	DLS03	1.45	−0.58		0.75	Syn		
60	Nd 2	4018.82	0.06	−0.850	DLS03	1.45	−0.58		0.75	Syn		
60	Nd 2	4021.33	0.32	−0.100	DLS03	1.45	−0.53		0.80	Syn		
60	Nd 2	4023.00	0.56	0.040	DLS03	1.45	−0.48		0.85	Syn		
60	Nd 2	4059.95	0.20	−0.520	DLS03	1.45	−0.58		0.75	Syn		
60	Nd 2	4061.08	0.47	0.550	DLS03	1.45	−0.61		0.72	Syn		
60	Nd 2	4069.26	0.06	−0.570	DLS03	1.45	−0.61		0.72	Syn		
60	Nd 2	4109.07	0.06	−0.160	DLS03	1.45	−0.63		0.70	Syn		
60	Nd 2	4109.45	0.32	0.350	DLS03	1.45	−0.63		0.70	Syn		
60	Nd 2	4135.32	0.63	−0.070	DLS03	1.45	−0.53		0.80	Syn		
60	Nd 2	4156.08	0.18	0.160	DLS03	1.45	−0.63		0.70	Syn		
60	Nd 2	4177.33	0.06	−0.100	DLS03	1.45	−0.62		0.71	Syn		
60	Nd 2	4385.66	0.20	−0.300	DLS03	1.45	−0.62		0.71	Syn		

Table 8. continued.

Z	Atom/ mol	λ (Å)	E_{exc} (eV)	$\log gf$	Ref	$\log \varepsilon$ Solar	$\log \varepsilon$ LTE	$\log \varepsilon$ NLTE	[X/Fe]	W_λ (mÅ)	$\log \Gamma_6/N_H$ (rad/s·cm^3)	Note, Ref.
1	2	3	4	5	6	7	8	9	10	11	12	13
60	Nd 2	4462.98	0.56	0.040	DLS03	1.45	−0.48		0.85	Syn		
60	Nd 2	4706.54	0.00	−0.710	DLS03	1.45	−0.56		0.77	Syn		
60	Nd 2	5212.35	0.20	−0.960	DLS03	1.45	−0.65		0.68	Syn		
60	Nd 2	5255.51	0.20	−0.670	DLS03	1.45	−0.53		0.80	Syn		
60	Nd 2	5319.82	0.55	−0.140	DLS03	1.45	−0.67		0.66	Syn		
62	Sm 2	3568.26	0.48	0.290	LDS06	1.00	−1.09		0.69	Syn		
62	Sm 2	3760.71	0.19	−0.400	LDS06	1.00	−0.89		0.89	Syn		
62	Sm 2	4318.94	0.28	−0.250	LDS06	1.00	−0.86		0.92	Syn		
62	Sm 2	4434.32	0.38	−0.070	LDS06	1.00	−0.96		0.82	Syn		
62	Sm 2	4467.34	0.66	0.150	LDS06	1.00	−0.84		0.94	Syn		
62	Sm 2	4519.63	0.54	−0.350	LDS06	1.00	−0.86		0.92	Syn		
63	Eu 2	3819.67	0.00	0.510	LWD01	0.52	−1.32	−1.17	1.09	Syn		HFS:LWD01
63	Eu 2	3907.11	0.21	0.170	LWD01	0.52	−1.27	−1.07	1.19	Syn		HFS:LWD01
63	Eu 2	4129.72	0.00	0.220	LWD01	0.52	−1.27	−1.12	1.14	Syn		HFS:LWD01
63	Eu 2	4205.02	0.00	0.210	LWD01	0.52	−1.29	−1.14	1.12	Syn		HFS:LWD01
64	Gd 2	3358.62	0.03	0.250	DLS06	1.11	−0.79		0.88	Syn		
64	Gd 2	3422.46	0.24	0.710	DLS06	1.11	−0.63		1.04	Syn		
64	Gd 2	3481.80	0.49	0.110	DLS06	1.11	−0.83		0.84	Syn		
64	Gd 2	3768.40	0.08	0.210	DLS06	1.11	−0.69		0.98	Syn		
64	Gd 2	3796.38	0.03	0.020	DLS06	1.11	−0.66		1.01	Syn		
64	Gd 2	4085.57	0.73	−0.010	DLS06	1.11	−0.77		0.90	Syn		
64	Gd 2	4130.37	0.73	0.140	DLS06	1.11	−0.73		0.94	Syn		
64	Gd 2	4215.02	0.43	−0.440	DLS06	1.11	−0.66		1.01	Syn		
65	Tb 2	3509.14	0.00	0.700	LWC01	0.28	−1.53		0.97	Syn		HFS:LWB01
65	Tb 2	3848.73	0.00	0.280	LWC01	0.28	−1.49		1.01	Syn		
66	Dy 2	3407.80	0.00	0.180	WLN00	1.13	−0.68		0.97	Syn		
66	Dy 2	3445.57	0.00	−0.150	WLN00	1.13	−0.56		1.09	Syn		
66	Dy 2	3454.32	0.10	−0.140	WLN00	1.13	−0.61		1.04	Syn		
66	Dy 2	3460.97	0.00	−0.070	WLN00	1.13	−0.56		1.09	Syn		
66	Dy 2	3506.81	0.10	−0.600	WLN00	1.13	−0.71		0.94	Syn		
66	Dy 2	3531.71	0.00	0.770	WLN00	1.13	−0.63		1.02	Syn		
66	Dy 2	3534.96	0.10	−0.040	WLN00	1.13	−0.51		1.14	Syn		
66	Dy 2	3536.02	0.54	0.530	WLN00	1.13	−0.64		1.01	Syn		
66	Dy 2	3538.52	0.00	−0.020	WLN00	1.13	−0.64		1.01	Syn		
66	Dy 2	3550.22	0.59	0.270	WLN00	1.13	−0.54		1.11	Syn		
66	Dy 2	3563.15	0.10	−0.360	WLN00	1.13	−0.59		1.06	Syn		
66	Dy 2	3694.81	0.10	−0.110	WLN00	1.13	−0.66		0.99	Syn		
66	Dy 2	3944.68	0.00	0.110	WLN00	1.13	−0.57		1.08	Syn		
66	Dy 2	3996.69	0.59	−0.260	WLN00	1.13	−0.57		1.08	Syn		
66	Dy 2	4077.96	0.10	−0.040	WLN00	1.13	−0.51		1.14	Syn		
67	Ho 2	3398.94	0.00	0.410	LSC04	0.51	−1.37		0.90	Syn		HFS:LSC04
67	Ho 2	3416.44	0.08	0.260	LSC04	0.51	−1.45		0.82	Syn		HFS:LSC04
67	Ho 2	3456.00	0.00	0.760	LSC04	0.51	−1.30		0.97	Syn		HFS:LSC04
67	Ho 2	3796.67	0.00	0.160	LSC04	0.51	−1.19		1.08	Syn		HFS:LSC04
67	Ho 2	3810.00	0.00	0.190	LSC04	0.51	−1.22		1.05	Syn		HFS:LSC04
68	Er 2	3499.10	0.06	0.290	LSC08	0.96	−0.89		0.93	Syn		
68	Er 2	3559.89	0.00	−0.690	LSC08	0.96	−0.90		0.92	Syn		
68	Er 2	3616.57	0.00	−0.310	LSC08	0.96	−0.73		1.09	Syn		
68	Er 2	3633.54	0.00	−0.530	LSC08	0.96	−0.91		0.91	Syn		
68	Er 2	3692.65	0.06	0.280	LSC08	0.96	−0.79		1.03	Syn		
68	Er 2	3729.52	0.00	−0.590	LSC08	0.96	−0.66		1.16	Syn		
68	Er 2	3786.84	0.00	−0.520	LSC08	0.96	−0.73		1.09	Syn		
68	Er 2	3830.48	0.00	−0.220	LSC08	0.96	−0.84		0.98	Syn		
68	Er 2	3896.23	0.06	−0.120	LSC08	0.96	−0.89		0.93	Syn		
68	Er 2	3906.31	0.00	0.120	LSC08	0.96	−0.74		1.08	Syn		
68	Er 2	3938.63	0.00	−0.520	KB95	0.96	−0.76		1.06	Syn		
69	Tm 2	3462.20	0.00	0.030	WL97b	0.14	−1.68		0.96	Syn		

Table 8. continued.

Z	Atom/ mol	λ (Å)	E_{exc} (eV)	$\log gf$	Ref	$\log\varepsilon$			[X/Fe]	W_λ (mÅ)	$\log\Gamma_6/N_H$ (rad/s·cm^3)	Note, Ref.
						Solar	LTE	NLTE				
1	2	3	4	5	6	7	8	9	10	11	12	13
69	Tm 2	3700.26	0.03	−0.380	WL97b	0.14	−1.61		1.03	Syn		
69	Tm 2	3701.36	0.00	−0.540	WL97b	0.14	−1.63		1.01	Syn		
69	Tm 2	3795.76	0.03	−0.230	WL97b	0.14	−1.55		1.09	Syn		
69	Tm 2	3848.02	0.00	−0.140	WL97b	0.14	−1.76		0.88	Syn		
70	Yb 2	3694.19	0.00	−0.300	BDM98	0.86	−1.03		0.89	Syn		HFS:MGH94
72	Hf 2	3399.79	0.00	−0.570	LDL07	0.88	−1.32		0.58	Syn		
76	Os 1	4260.85	0.00	−1.430	IAN03	1.45	−0.17		1.16	Syn		
77	Ir 1	3513.65	0.00	−1.210	IAN03	1.38	−0.04		1.36	Syn		HFS:CSB05
77	Ir 1	3800.12	0.00	−1.440	IAN03	1.38	−0.05		1.35	Syn		HFS:CSB05
90	Th 2	4019.13	0.00	−0.228	NZL02	0.08	−1.67		1.03	Syn		

ABO Anstee & O'Mara (1995); Barklem & O'Mara (1997); Barklem et al. (1998); Barklem & O'Mara (1998); Barklem & Aspelund-Johansson (2005);
BBP89 Blackwell et al. (1989);
BBH83 Borghs et al. (1983);
BCB05 Barklem et al. (2005);
BDM98 Biémont et al. (1998);
BG80 Biémont & Godefroid (1980);
BHN93 Bizzarri et al. (1993);
BKK91 Bard et al. (1991);
BL91 O'Brian & Lawler (1991);
CSB05 Cowan et al. (2005);
CSS82 Cardon et al. (1982);
DLS03 Den Hartog et al. (2003);
DLS06 Den Hartog et al. (2006);
FMW88 Fuhr et al. (1988);
FW96 Fuhr & Wiese (1996);
G89 Ginibre (1989);
GLS04 Gehren et al. (2004);
HLG82 Hannaford et al. (1982);
HS80 Huber & Sandeman (1980);
HSR99 Holt et al. (1999);
IAN03 Ivarsson et al. (2003);
ILW01 Ivarsson et al. (2001);
K94 Kurucz (1994);
KB95 Kurucz & Bell (1995);
KG00 Kling & Griesmann (2000);
LBS01 Lawler et al. (2001a);
LD89 Lawler & Dakin (1989);
LDL07 Lawler et al. (2007);
LDS06 Lawler et al. (2006);
LGB03 Lefébvre et al. (2003);
LSC04 Lawler et al. (2004);
LSC08 Lawler et al. (2008);
LSC09 Lawler et al. (2009);
LNA06 Ljung et al. (2006);
LWB01 Lawler et al. (2001d);
LWC01 Lawler et al. (2001c);
LWD01 Lawler et al. (2001b);
M98 McWilliam (1998);
MB09 Meléndez & Barbuy (2009);
MBM06 Malcheva et al. (2006);
MFW88 Martin et al. (1988);
MGH94 Mårtensson-Pendrill et al. (1994);
MKP07 Mashonkina et al. (2007a);
MPS95 McWilliam et al. (1995);
MZG08 Mashonkina et al. (2008);
NBI98 Nörtershäuser et al. (1998);
NIST8 Ralchenko et al. (2008);

NKW99 Nitz et al. (1999);
NZL02 Nilsson et al. (2002);
OWL91 O'Brian et al. (1991);
P96 Pickering (1996);
PTP01 Pickering et al. (2001);
RCW80 Reader et al. (1980);
S81 Smith (1981);
SON75 Smith & O'Neil (1975);
SR81 Smith & Raggett (1981);
SRE95 Sansonetti et al. (1995);
Th89 Theodosiou (1989);
WF75 Wiese & Fuhr (1975);
WL97a Wickliffe & Lawler (1997a);
WL97b Wickliffe & Lawler (1997b);
WLN00 Wickliffe et al. (2000);
XSD06 Xu et al. (2006).